

VELOCITY ANALYSIS OF MULTI-RECEIVER FULL WAVEFORM ACOUSTIC LOGGING DATA IN OPEN AND CASED HOLES

by

Lisa V. Block, C.H. Cheng, and Gregory L. Duckworth

Earth Resources Laboratory
Department of Earth, Atmospheric, and Planetary Sciences
Massachusetts Institute of Technology
Cambridge, MA 02139

ABSTRACT

Average semblance and maximum-likelihood spectral analysis are applied to synthetic full waveform acoustic logging data to determine formation velocities. Of particular interest is the ability of these methods to resolve the P wave and pseudo-Rayleigh wave arrivals in data from poorly-bonded cased boreholes. In open-hole data the velocity analyses generally yield results within 0.15 km/s of the true velocities. For cased-hole models with no steel/cement bonding (free pipe), the measured P-wave velocities are 0.2 to 0.6 km/s less than the actual formation velocities, and the S-wave velocities are within 0.15 km/s of the true velocities. If the P-wave velocity is fairly close to the plate velocity of the steel pipe (within 0.7 km/s or so), then the P-wave arrival is not separated from the steel arrival by the semblance method, but the P wave is resolved by the spectral analysis. For cased-hole models with no cement/formation bonding (unbonded casing), accurate formation velocities are obtained if the velocities are not too great. When the formation P-wave velocity approaches the velocity of the casing arrival, the P-wave resolution is lost by both methods. Further work needs to be done to better define this limit.

INTRODUCTION

Formation velocities are easily obtained from full waveform acoustic well logs recorded in open boreholes by measuring the moveout times of the P wave and pseudo-Rayleigh wave between two receivers. This method can also be applied to acoustic well logs recorded in well-bonded cased holes (Tubman et al., 1984). However, if the steel pipe is not bonded to the cement, or if the cement is not bonded to the formation, the P wave is often completely obscured by a casing arrival. This casing arrival may also interfere with the pseudo-Rayleigh wave, making determination of the formation S-wave velocity difficult. This paper addresses the problem of determining formation velocities from full waveform acoustic well logs recorded in poorly-bonded cased holes. Two methods of velocity

analysis are employed — average semblance and spectral analysis using the maximum-likelihood method. Hsu and Baggeroer (1986) recently demonstrated the feasibility of applying the maximum-likelihood method to multi-receiver acoustic logging data and compared this spectral analysis method to the semblance method. Here a systematic approach is taken to evaluate the application of these methods of velocity analysis to acoustic logging data from poorly-bonded cased boreholes. First these methods are applied to open-hole synthetic data to determine the quality of the results under optimal conditions. Then the velocity analysis techniques are applied to synthetic data from cased holes with no steel/cement bonding (the free pipe situation) and to synthetic data from cased holes with no cement/formation bonding (the unbonded casing situation). For both situations, models with varying formation velocities and borehole geometries are studied. Finally, field data from an open hole is analyzed. Field data from cased boreholes will be studied in the future.

VELOCITY ANALYSIS

Two types of velocity analysis are implemented. One of these is a spectral velocity analysis technique which consists of calculating a two-dimensional Fourier transform within a short time window of given moveout across the receiver array. An example of such a window is shown in Figure 1. τ is the beginning time of the window on the near trace, T is the length of the window, and p is the slope (dt/dx) of the window. The slope p is equal to the slowness in the direction of the array. For receivers in a borehole, the signals travel essentially parallel to the array, and hence p is equal to the inverse of the velocity of propagation. For a fixed time τ , Fourier transforms are calculated for many different slownesses. The window is then advanced by an amount $d\tau$, and the process is repeated. The final result is a series of contour plots of the power spectrum. Each plot is a function of time τ and velocity, $1/p$, for a small band of frequencies. Since the calculations are made at equal increments of p , the velocity axis is linear in slowness. The width of the frequency bands, df , is inversely proportional to the length of the FFT used to implement the Fourier transforms. To determine the length of the FFT, the window of length T is padded with zeros until the total number of samples is a power of 2. Hence, the width of the frequency bands depends upon the sampling interval of the data as well as the window length T . After trying various window lengths, a length of 250 μ s was decided upon for the synthetic data. This length is used for all models. However, the sampling interval is not the same for all of the data sets, and therefore the frequency bands are slightly different for different models. In this paper "the velocity spectrum at f_o " refers to the contour plot of the power spectrum for a band of frequencies centered at f_o . The width of the frequency band varies from model to model and is given in the figure caption. The array processing is implemented with the maximum-likelihood method to obtain high-resolution results. Details of this technique are presented in Duckworth (1983).

The second method of velocity analysis is the average semblance. The average

semblance is the ratio of the energy of a stacked trace to the sum of the energies of the individual traces within a time window, divided by the number of traces. The beginning time τ and slope p of the window are varied as in the spectral analysis. Hence, the result is a contour plot of the average semblance as a function of τ and velocity ($1/p$). This can be expressed by:

$$Semblance_{avg}(\tau, p) = \frac{\sum_{t=\tau+px}^{\tau+px+T} \left(\sum_{i=1}^N A_i(t) \right)^2}{N \sum_{t=\tau+px}^{\tau+px+T} \sum_{i=1}^N (A_i(t))^2}$$

where A_i is the amplitude response of the i^{th} receiver, x is the distance from the near receiver, and N is the number of receivers.

SYNTHETIC DATA

Cased boreholes can be modelled by concentric layers surrounding a fluid-filled cylinder. Each layer has constant density, P-wave and S-wave velocities, and P-wave and S-wave attenuation factors. The outermost layer is infinite in extent. In a well-bonded cased hole, the steel pipe surrounding the borehole fluid is bonded to a layer of cement, which in turn is bonded to the formation. In the free pipe situation, the pipe is not bonded to the cement. This situation is modelled by inserting a fluid layer between the steel and cement layers. If the steel pipe is bonded to the cement but the cement is not bonded to the formation, the situation is referred to as the unbonded casing situation. For this case a fluid layer is inserted between the cement layer and the outermost, infinite layer representing the formation.

Tubman (1984) developed a method which employs a Thomson-Haskell type propagator matrix to relate displacements and stresses across these concentric layers. Synthetic microseismograms are then generated with the method of discrete wavenumber integration. The data presented in this report consists of sets of either eleven or twelve microseismograms representing arrays of receivers. The near receiver is either 3.05 m (10 ft) from the source (for the eleven-receiver array) or 2.90 m (9.5 ft) from the source (for the twelve-receiver array). The receiver spacing is 15.24 cm (0.5 ft). The actual borehole radius is 10.16 cm (4.0 inches) for all of the models. For the cased hole models, the inner borehole radius (distance to the steel pipe) is 4.7 cm (1.85 inches). The densities, velocities, and attenuation factors of the fluid, steel, and cement layers remain constant. The thickness of the steel layer is constant (1.016 cm or 0.4 inches). Fluid layers are added on either side of the cement by decreasing the thickness of the cement layer. The center frequency of the source function is 13 kHz, and a bandpass filter is applied to restrict the frequency content between approximately 5 and 18 kHz.

RESULTS

Open Hole

Data for an open borehole model are shown in Figure 2. The two distinct wave packets are those of the P wave and the pseudo-Rayleigh wave. The pseudo-Rayleigh wave exhibits normal dispersion. The lowest frequencies of this wave travel with the formation S-wave velocity. Hence, the S wave cannot be seen, but the formation S-wave velocity can be determined from velocity analysis of the pseudo-Rayleigh wave. The Stoneley wave, which travels at a velocity slightly less than that of the borehole fluid, is also obscured by the pseudo-Rayleigh wave. The formation P-wave velocity for this model is 4.00 km/s, and the S-wave velocity is 2.13 km/s.

Velocity spectra at frequencies of 4, 8, and 16 kHz are shown in Figures 3a-c, and Figure 3d contains the semblance contour plot. In all cases there is a peak corresponding to the P wave at a velocity of about 3.95 km/s. Hence, an accurate formation P-wave velocity is obtained. In the spectrum at 4 kHz (Figure 3a), the pseudo-Rayleigh wave is represented by a maximum at a time of 1.5 ms and a velocity of 2.10 km/s. At 8 kHz (Figure 3b), the peak is located at 1.7 ms and 2.05 km/s, and at 16 kHz (Figure 3c), the peak occurs at 1.9 ms and approximately 2.02 km/s. This slight decrease in velocity, and corresponding increase in arrival time, with increasing frequency demonstrates the dispersive nature of the pseudo-Rayleigh wave. The best estimate of the formation S-wave velocity (2.10 km/s, compared to the actual velocity of 2.13 km/s) is obtained from the lowest frequency band as expected. At 4 kHz, below its cutoff frequency, the pseudo-Rayleigh wave is not excited. However, as pointed out by Paillet and Cheng (1986), there is refracted S wave energy propagating. This apparently is what is being detected. The semblance plot in Figure 3d also yields a pseudo-Rayleigh wave velocity, or S-wave velocity, of 2.10 km/s. Although the Stoneley wave cannot be identified on the microseismograms, it is resolved by spectral velocity analysis at 4 kHz. This Stoneley wave maximum occurs at a velocity of about 1.47 km/s (Figure 3a), corresponding to the theoretical Stoneley wave velocity. (The borehole fluid velocity is 1.68 km/s.) This arrival is not resolved in the velocity spectra at higher frequencies or in the semblance plot.

The dispersion of the pseudo-Rayleigh wave noted above is not noticeable in most of the following cases for several reasons. First, the maximum corresponding to the pseudo-Rayleigh wave is often not as well resolved as in this simple model. Also, since the velocity axis is linear in slowness, the higher the formation velocities, the more difficult it is to see minor changes in velocity. Perhaps most importantly, in cased hole models the effective borehole radius is decreased, resulting in a shift of the dispersion curves to higher frequencies (Cheng and Toksöz, 1981). Hence, there is less dispersion over the frequency range of the source function for cased hole models than for open hole models.

The relatively small maxima in the lower left corners of the plots in Figures 3b-d are due to cycle-skipping across the P-wave arrival. The velocity of these maxima (approximately 1.25 km/s) is such that one cycle of the waveform is skipped from one receiver to the next. In other words, a peak on one trace is being aligned with the following peak on the next trace. The misaligned waveforms add constructively, resulting in the observed maxima. This cycle-skipping phenomenon occurs in nearly all of the semblance plots presented in this paper, and in some of the velocity spectra. It is generally more prominent in cased boreholes than in open holes due to the long duration of the casing arrival.

The data in Figure 4 is from an open hole model with high formation velocities. The P-wave velocity is 5.94 km/s, and the S-wave velocity is 3.20 km/s. The nature of the pseudo-Rayleigh wave has changed since its dispersion curves depend upon the formation S-wave velocity. Once again the Stoneley wave is difficult to identify.

The results of the velocity analysis are presented in Figures 5a-d. In the velocity spectrum at 4 kHz (Figure 5a), the P-wave and pseudo-Rayleigh wave maxima have poor resolution. That is, the precise velocities at which the peaks occur is not clear. The P-wave peak lies between about 5.60 and 5.95 km/s, and the pseudo-Rayleigh wave peak occurs between 3.10 and 3.25 km/s. This is probably the result of the band-pass filter on the synthetic microseismograms. At 8 kHz (Figure 5b) these maxima are better resolved. The P-wave peak is centered at 5.85 km/s, and the peak associated with the pseudo-Rayleigh wave occurs at 3.10 km/s. The P-wave maximum remains well-resolved at higher frequencies (and occurs at the same velocity), but the pseudo-Rayleigh wave maximum becomes fragmented. At 16 kHz (Figure 5c) the pseudo-Rayleigh wave is represented by four peaks lying between 3.10 and 3.25 km/s. In the semblance plot of Figure 5d, the P-wave maximum is centered at 5.80 km/s, and the pseudo-Rayleigh wave maximum has two main subpeaks at 3.10 km/s and 3.25 km/s. In short, the velocity resolution is not as good for this model as for the previous one. However, good formation velocities are still obtained.

The Stoneley wave is represented by a maximum at 1.60 km/s in the velocity spectrum at 4 kHz. It does not appear on the spectra at higher frequencies, but a small maximum does occur in the semblance plot at 1.60 km/s. This velocity is consistent with the theoretical Stoneley wave velocity of 1.57 km/s in this formation.

Free Pipe

Figure 6 shows microseismograms for a cased borehole model with a 1.27 cm-thick fluid layer between the steel and cement. The formation P-wave velocity is 4.00 km/s, and the S-wave velocity is 2.13 km/s. The first arrival is that of a disturbance traveling through the steel. This arrival completely obscures the P wave. The pseudo-Rayleigh arrival is clear. In contrast to open hole data, the Stoneley wave is easily identified. As

noted earlier, the presence of the casing decreases the effective radius of the borehole, thereby increasing the cut-off frequency of the pseudo-Rayleigh wave. Thus, the pseudo-Rayleigh wave is excited to a lesser extent, and the Stoneley wave is more dominant in the cased hole models than in the open hole models.

Figures 7a–c contain the velocity spectra for frequencies of 8, 12, and 16 kHz, respectively. Four peaks can be clearly seen in Figure 7a. The broad peak centered at 0.55 ms and having a velocity between 5.1 and 5.3 km/s corresponds to the steel arrival. The peak at 1 ms with a velocity of 3.75 km/s represents the P wave. This velocity is a little less than the actual formation P-wave velocity of 4.00 km/s. The pseudo-Rayleigh wave comes in at about 1.5 ms with a velocity of 2.15 km/s, extremely close to the true S-wave velocity of 2.13 km/s. The Stoneley wave is represented by the large maximum at 1.8 ms and 1.55 km/s. This is different from the Stoneley wave velocity in an open formation. At 12 kHz (Figure 7b) the peak associated with the pseudo-Rayleigh arrival is more distinct than at 8 kHz, and it has a somewhat lower velocity of 2.05 km/s. The resolution of the P wave and Stoneley wave is less at 12 kHz than at 8 kHz, but the velocities are consistent. At 16 kHz (Figure 7c) the Stoneley arrival has nearly disappeared, and there are two peaks representing the P wave (at 3.75 km/s) rather than one. The pseudo-Rayleigh maximum is still clear, at a velocity of 2.05 km/s.

The semblance is presented in Figure 7d. The steel arrival, P wave, and Stoneley wave appear as strong peaks with the same velocities as in the velocity spectra. (The Stoneley arrival is located at 1.8 ms. The linear feature to the left of the Stoneley wave is due to cycle-skipping across the steel arrival.) The peak representing the pseudo-Rayleigh arrival has a velocity of 2.07 km/s, about the same value as was measured from the velocity spectra at 12 and 16 kHz.

Microseismograms for the case of a very thin fluid layer (0.025 mm thick), referred to as a microannulus, are presented in Figure 8. The formation P-wave and S-wave velocities are the same as in the last situation, 4.00 km/s and 2.13 km/s, respectively. The first arrival still corresponds to a disturbance propagating through the steel, and the P-wave arrival cannot be seen. The nature of the steel arrival has changed, however. The first part of the waveform has fairly low amplitude, but the amplitude increases shortly before the arrival of the pseudo-Rayleigh wave. Hence, the pseudo-Rayleigh arrival is not as clear in this case as formerly.

The velocity spectra look very similar at all of the frequencies examined, and thus one representative plot is shown in Figure 9a. A plot of the semblance is shown in Figure 9b. In both figures peaks representing the P wave and pseudo-Rayleigh wave occur at velocities of about 3.75 km/s and 2.10 km/s, respectively. The P-wave velocity is the same as that measured previously. In this case the measured pseudo-Rayleigh wave velocity is nearly constant with frequency (varying by not more than 0.02 km/s over a range of about 9 kHz), and is consistent with the velocities determined for the last model. The peak corresponding to the steel arrival yields a velocity of about 5.55 km/s, somewhat higher than the velocity measured previously (5.1–5.3 km/s). In short,

the thickness of the fluid layer does not affect the measured formation velocities in this case, but does influence the velocity of the steel arrival.

Models having the same geometries as those just discussed but having higher formation velocities are examined. The P-wave velocity for these models is 4.88 km/s, and the S-wave velocity is 2.60 km/s. The data for the case with the thicker fluid layer (1.27 cm) is presented in Figure 10. The duration of the steel arrival is greater than in the corresponding model with the lower velocities, and therefore the pseudo-Rayleigh arrival is not as clear as previously.

The velocity spectra and semblance are shown in Figures 11a-d. The maximum in the extreme upper left corner of Figure 11a (velocity spectra at 8 kHz) is due to slight noncausality in the synthetic data. The true steel arrival corresponds to the peak at 0.6 ms and 5.3 km/s. The P wave is represented by a small peak at 1.05 ms and 4.5 km/s. Again, the measured P-wave velocity is less than the actual velocity. These two maxima begin to merge with increasing frequency. At 16 kHz (Figure 11c) the steel arrival is located at 0.8 ms and 5.1 km/s. The P-wave maximum has moved to 1.0 ms and approximately 4.65 km/s. The pseudo-Rayleigh wave is associated with a distinct peak at a velocity of about 2.45 km/s at all frequencies shown, somewhat less than the actual S-wave velocity of 2.60 km/s. The semblance plot in Figure 11d yields the same S-wave velocity. However, no distinct P-wave maximum is present. The steel arrival and the P wave are represented by a linear feature varying in velocity from 4.3 km/s to 5.4 km/s. Apparently the P-wave formation velocity is close enough to the plate velocity of steel to cause minor resolution problems in the frequency domain and a total loss of resolution in the time domain.

The Stoneley wave maximum occurs at a velocity of 1.55 km/s, the same velocity as determined for the model with the slower formation velocities. This fact agrees with the observation made by Tubman et al. (1984) that the casing, rather than the formation velocities, is the major influence on the Stoneley wave velocity. In fact, the Stoneley wave velocity remains essentially constant in all of the cased hole models studied here. (Recall that the steel and cement velocities and the thickness of the steel layer are constant in all of the models.) Hence, little will be said concerning the Stoneley wave in the remainder of the paper.

Microseismograms generated from the model with the microannulus are shown in Figure 12. The pseudo-Rayleigh arrival is totally obscured in this case. A representative velocity spectrum is shown in Figure 13a, and the semblance is presented in Figure 13b. The pseudo-Rayleigh arrival appears the same as in the last case, corresponding to a peak at 2.45 km/s. However, the behavior of the steel and P-wave maxima has changed. The two maxima do not begin to merge with increasing frequency, and the velocities at which they occur are different than previously. The P-wave maximum occurs at a velocity of 4.3 km/s (at all frequencies examined). This velocity is 0.2 to 0.35 km/s less than that determined in the previous case and 0.58 km/s less than the actual formation P-wave velocity. The steel arrival maximum yields a velocity of 5.5 km/s, rather than

5.1 to 5.3 km/s as in the last case. The linear feature associated with the steel and P-wave arrivals on the semblance plot also spans a broader velocity range — 4.0 to 5.5 km/s, compared to 4.3 to 5.4 km/s previously. Thus, the thickness of the fluid layer does not affect the measured S-wave velocity, but does affect the measured P-wave and steel arrival velocities. Apparently when the formation P-wave velocity is fairly close to the plate velocity of the steel, the velocity analyses become more sensitive to changes in the geometry of the casing.

Unbonded Casing

Good steel/cement bonding but no cement/formation bonding, referred to as the unbonded casing situation, is modelled by inserting a fluid layer between the cement and the formation. Tubman (1984) showed that if the cement is sufficiently thick (on the order of 4 cm), it will damp out the steel arrival, and the P-wave arrival can be seen. However, if the cement is too thin, the first arrival on the microseismograms will be due to a disturbance propagating through the casing with a velocity intermediate between the steel and cement velocities. This situation can be observed in Figure 14. In this model, the thickness of the cement is 1.27 cm, and the thickness of the fluid layer is 3.18 cm. The complex nature of the first arrival is due to the combined ringing of the steel and the cement (Tubman, 1984). The amplitude variation within this arrival often causes its associated maxima on the velocity spectra to contain several subpeaks. The P-wave arrival is again completely obscured, and the pseudo-Rayleigh arrival is not clear. The formation P-wave velocity for this model is 4.00 km/s, and the S-wave velocity is 2.13 km/s.

Figures 15a–b contain a typical velocity spectrum and the semblance plot. The maximum representing the pseudo-Rayleigh wave occurs at a velocity of about 2.08 km/s on the velocity spectrum and 2.15 km/s on the semblance plot. Hence, a good formation S-wave velocity is obtained. The peak located at a velocity of about 4.65 km/s on the figures corresponds to the casing arrival. There is no peak representing the P wave on either the velocity spectrum or the semblance plot. Apparently these velocity analysis techniques are not powerful enough to separate the P-wave arrival from the complex casing arrival for this model.

The data in Figure 16 are from a model with the same casing parameters as previously, but the formation is slow. Since the formation S-wave velocity is less than the velocity of the borehole fluid, no pseudo-Rayleigh wave is generated. The casing arrival has the same appearance as before, and the P wave cannot be identified. The P-wave velocity of the formation is 2.90 km/s.

The two velocity spectra and the semblance plot in Figures 17a–c exhibit maxima at about 4.65 km/s as in the last case, verifying that this peak corresponds to a casing arrival. A strong peak representing the P wave is seen on the semblance plot, and smaller

maxima occur on the velocity spectra. The P-wave velocity measured from these plots is between 2.90 and 2.95 km/s. Hence, an accurate formation P-wave velocity is obtained for this model. Further work needs to be done to determine how close the formation P-wave velocity can be to the casing velocity before the P-wave resolution is lost.

Field Data

The data in Figure 18 was recorded with Schlumberger's Ridgefield tool in an open hole. This tool has twelve receivers. The near receiver is 3.96 m (13 ft) from the source, and the receiver spacing is 15.24 cm (0.5 ft). In this case the P-wave, pseudo-Rayleigh wave, and Stoneley wave arrivals are clear.

A typical velocity spectrum is shown in Figure 19a, and the semblance is presented in Figure 19b. The P wave, pseudo-Rayleigh wave, and Stoneley wave are well-resolved by both methods. A P-wave velocity of about 4.25 km/s and a Stoneley wave velocity of 1.45 km/s are measured. The pseudo-Rayleigh wave maximum occurs at 2.40 km/s on the velocity spectrum and 2.35 km/s on the semblance plot.

CONCLUSIONS

The average semblance and the maximum-likelihood spectral analysis yield good results for open-hole data. The resolution decreases slightly with increasing velocity, but in any case the measured velocities vary by not more than 0.15 km/s from the true velocities. For cased-hole models with no steel/cement bonding (free pipe), the measured formation P-wave velocities are approximately 0.2 to 0.6 km/s less than the actual velocities. Generally, the greater the formation P-wave velocity, the poorer the velocity estimate. Also, when the formation P-wave velocity is relatively close to the steel velocity, the P-wave arrival cannot be separated from the steel arrival by the semblance method. The two arrivals are resolved by spectral analysis, although the quality of resolution may vary with frequency. Furthermore, the measured P-wave velocity is sensitive to changes in the thickness of the fluid layer between the steel and the cement when the P-wave and steel velocities are close. In all cases (regardless of the formation velocities), decreasing the thickness of the fluid layer increases the measured velocity of the steel arrival. The accuracy of the measured S-wave velocities for the free pipe situation varies from excellent to 0.15 km/s less than the true velocities. The measured S-wave velocities are not influenced by the thickness of the fluid layer. For cased-hole models with no cement/formation bonding (unbonded casing), neither velocity analysis method can resolve the P-wave arrival when the P-wave velocity differs from the velocity of the casing arrival by 0.65 km/s. The P-wave velocity can be determined to an accuracy of about 0.05 km/s for slow formations. More work needs to be done to determine how close the formation P-wave velocity can be to the velocity of the casing arrival before the

P-wave resolution is lost. The formation S-wave velocity can be accurately measured by both methods in boreholes with unbonded casing.

The models presented here correspond to the simplest data sets (open boreholes) and the most complex data sets (poorly-bonded cased boreholes). Velocity analysis of the intermediate data sets, those from well-bonded cased holes, sometimes yields results as good as those from open holes and sometimes yields results which are somewhat poorer than open-hole data but better than poorly-bonded cased-hole data. Overall, the results from the study of synthetic data are encouraging. Analysis of field data from an open borehole also looks good. The next step is to apply these velocity analysis techniques to field data from cased boreholes. Also, these methods will be tested on synthetic data with fewer receivers and different receiver spacings.

REFERENCES

- Cheng, C. H., and Toksöz, M. N., 1981, Elastic wave propagation in a fluid-filled borehole and synthetic acoustic logs; *Geophysics*, 46, 1042-1053.
- Duckworth, G. L., 1983, Processing and inversion of Arctic Ocean refraction data; Sc.D. thesis, Joint Program in Ocean Engineering, Mass. Inst. Tech., Cambridge, Massachusetts, and Woods Hole Oceanographic Institution, Woods Hole, Massachusetts.
- Hsu, K., and Baggeroer, A. B., 1986, Application of the maximum-likelihood method (MLM) for sonic velocity logging; *Geophysics*, 51, 780-787.
- Paillet, F.L., and Cheng, C.H., 1986, A numerical investigation of head waves and leaky modes in fluid-filled boreholes; *Geophysics*, in press.
- Tubman, K. M., Cheng, C. H., and Toksöz, M. N., 1984, Synthetic full waveform acoustic logs in cased boreholes; *Geophysics*, 49, 1051-1059.
- Tubman, K. M., 1984, Full waveform acoustic logs in radially layered boreholes: Ph.D. thesis, Mass. Inst. Tech., Cambridge, Massachusetts.

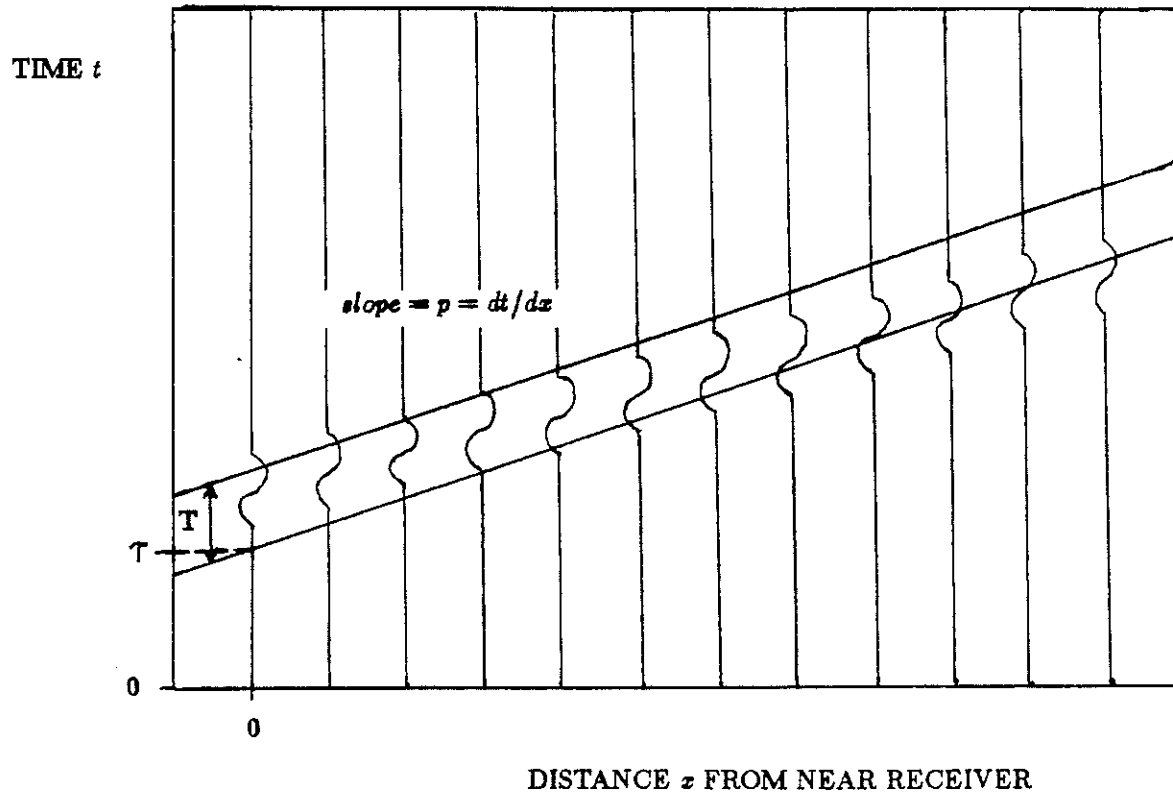
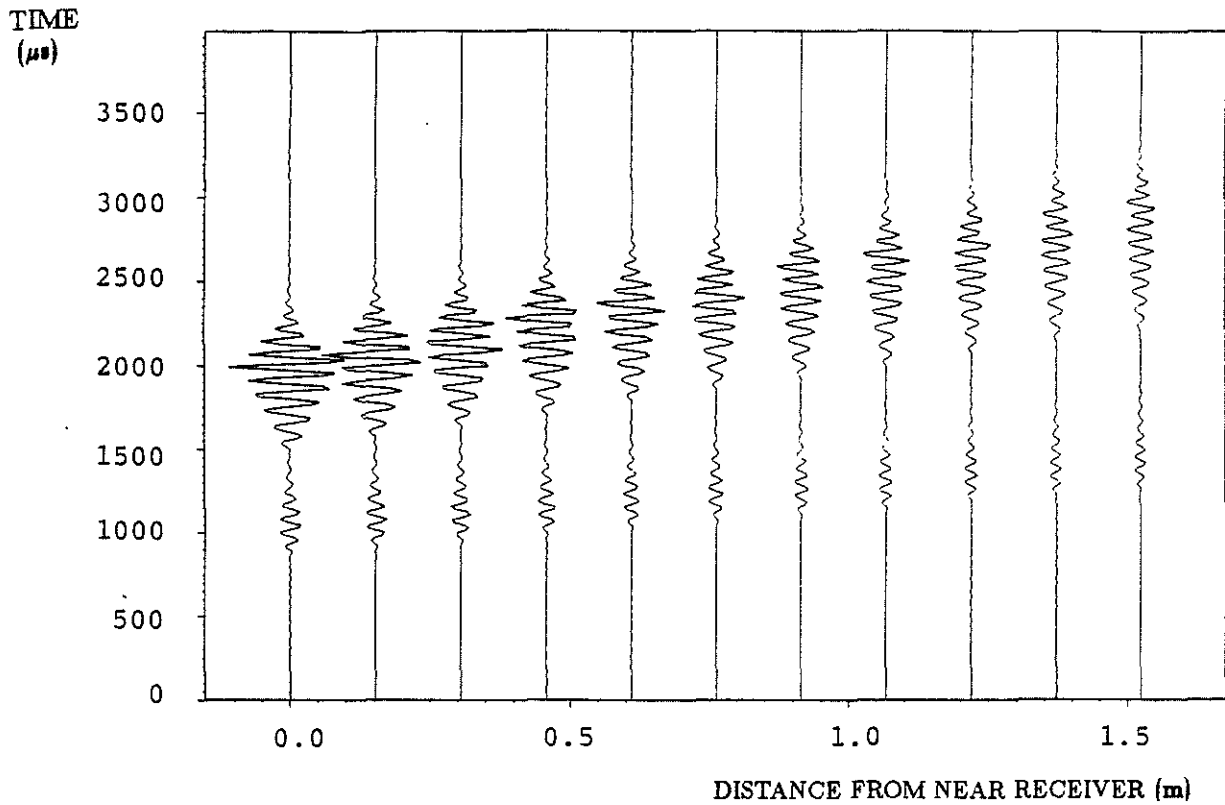


Figure 1: Window parameters.



MODEL PARAMETERS

LAYER	OUTER RADIUS (cm)	V_p (km/s)	V_s (km/s)	DENSITY (g/cc)	Q_p	Q_s
fluid	10.160	1.68	0.00	1.20	20.00	0.00
formation	∞	4.00	2.13	2.16	60.00	60.00

sampling interval = 15.625 μs

Figure 2: Data for an open borehole model.

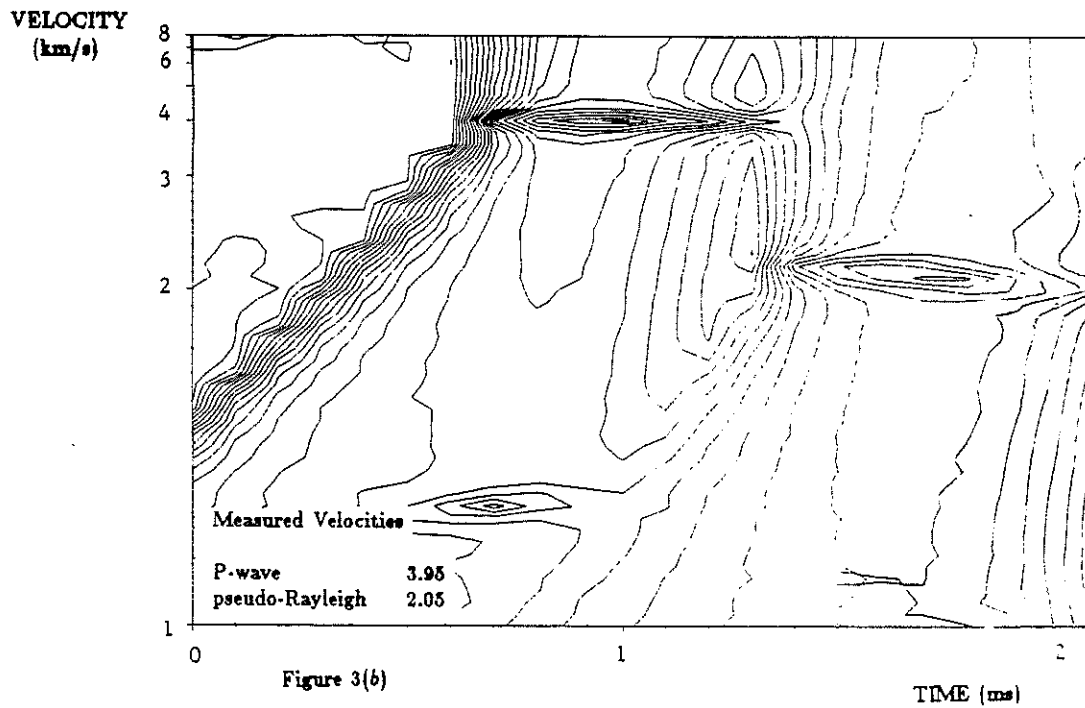
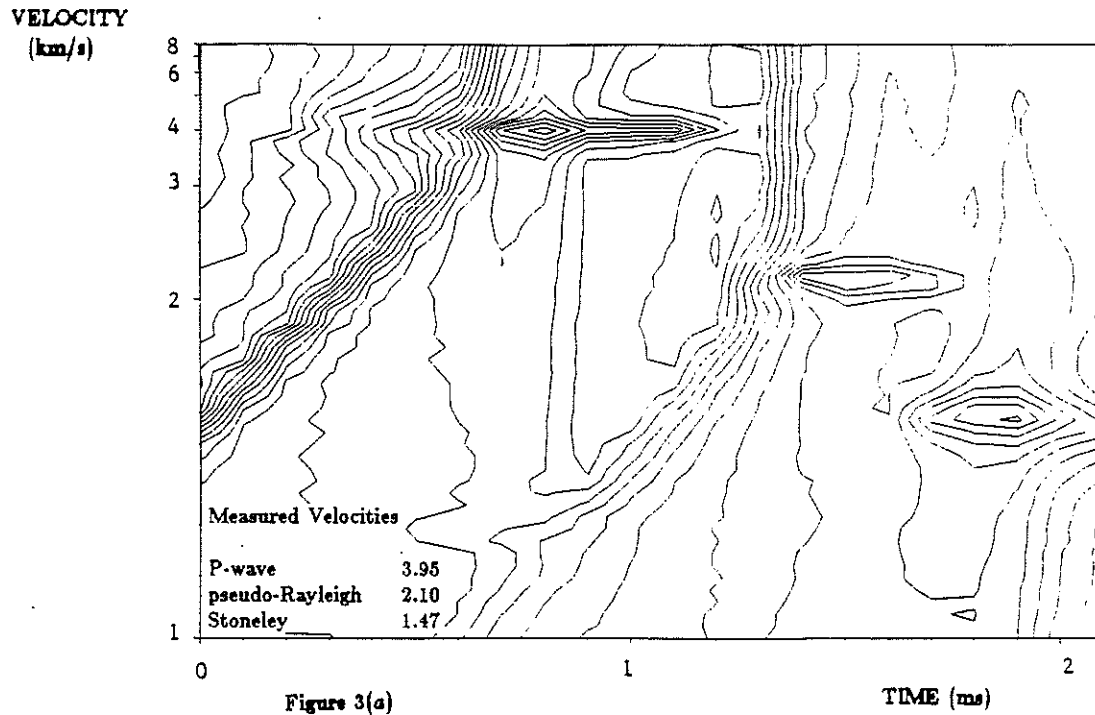
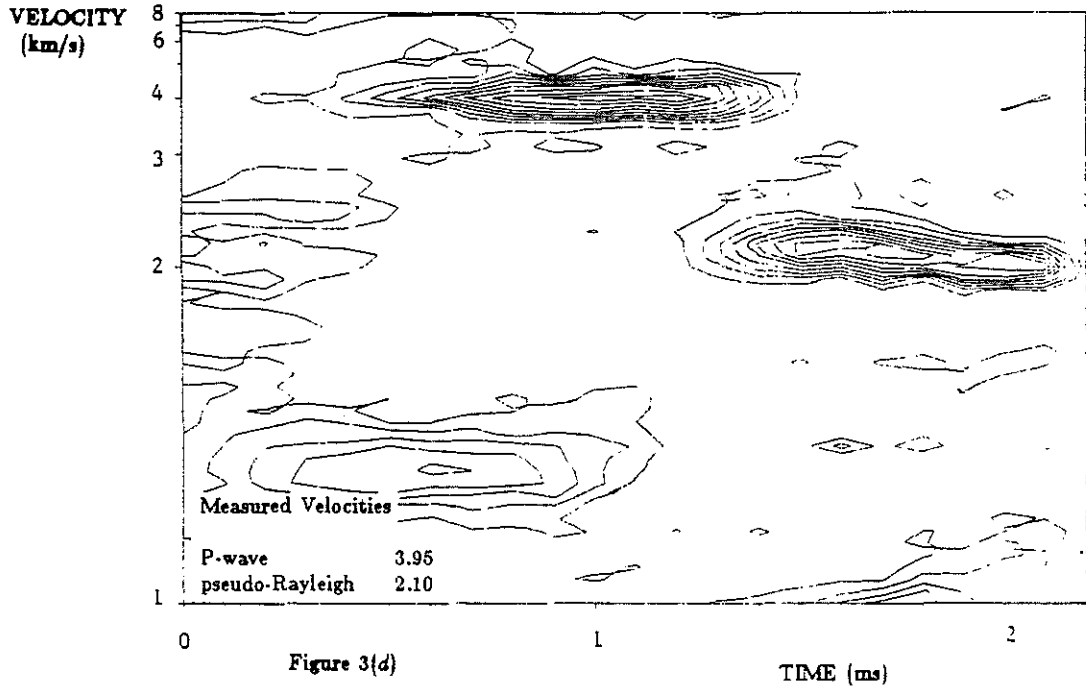
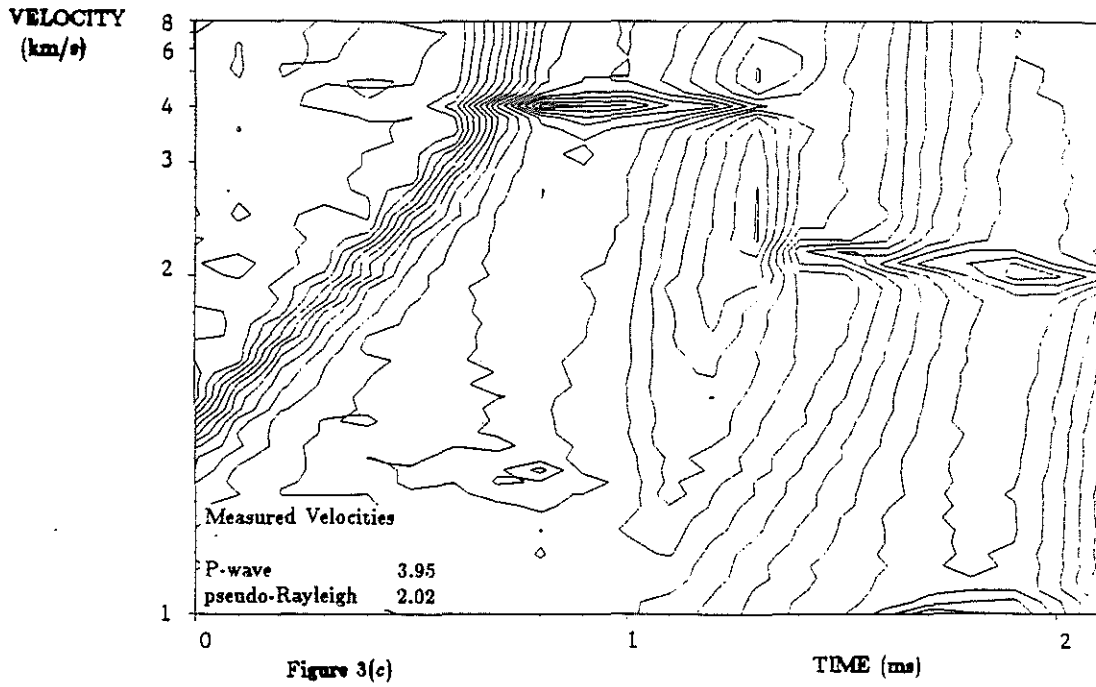
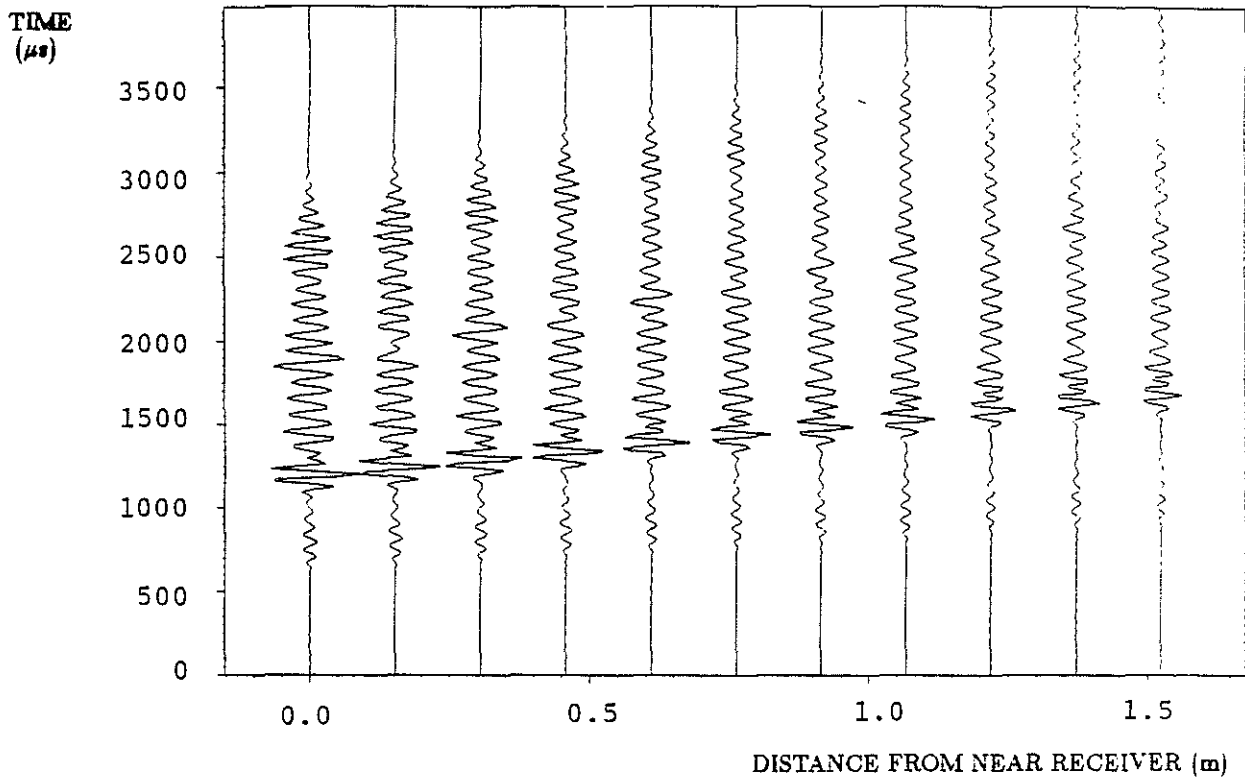


Figure 3: Velocity analysis for the model in Fig. 2. $T = 250 \mu\text{s}$; $dr = 100 \mu\text{s}$; $df = 4 \text{ kHz}$. (a) Velocity spectrum at 4 kHz. (b) Velocity spectrum at 8 kHz. (c) Velocity spectrum at 16 kHz. (d) Semblance.





MODEL PARAMETERS

LAYER	OUTER RADIUS (cm)	V_p (km/s)	V_s (km/s)	DENSITY (g/cc)	Q_p	Q_s
fluid	10.160	1.68	0.00	1.20	20.00	0.00
formation	∞	5.94	3.20	2.30	95.00	69.00

sampling interval = 15.625 μs

Figure 4: Data for an open borehole model with high formation velocities.

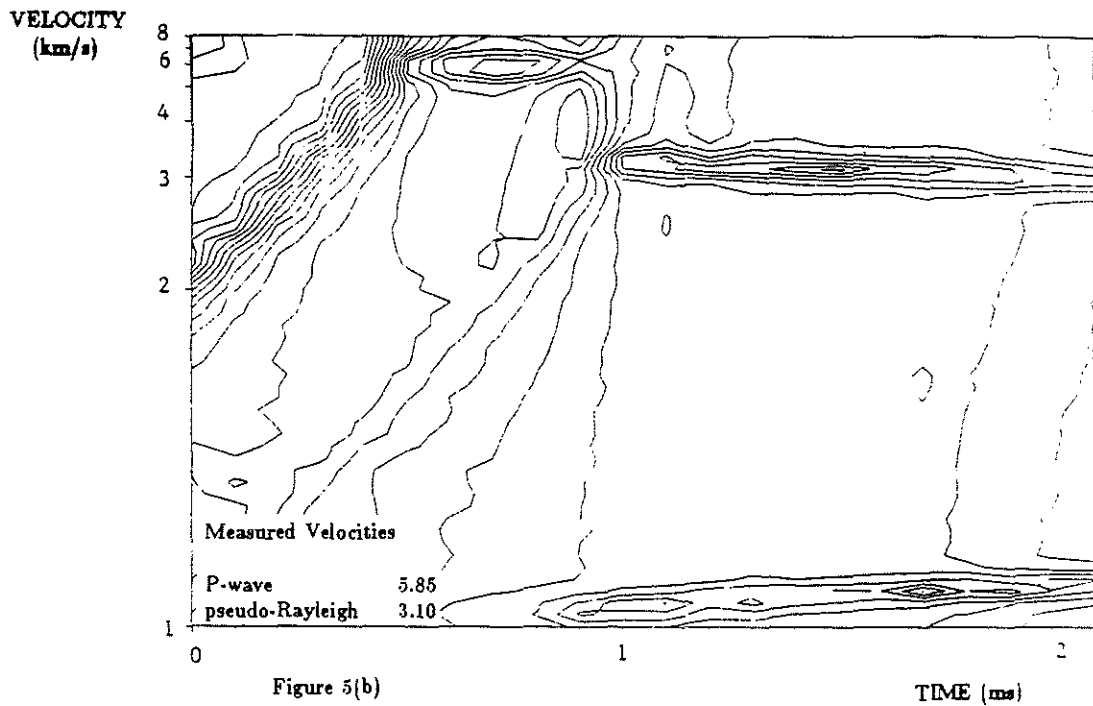
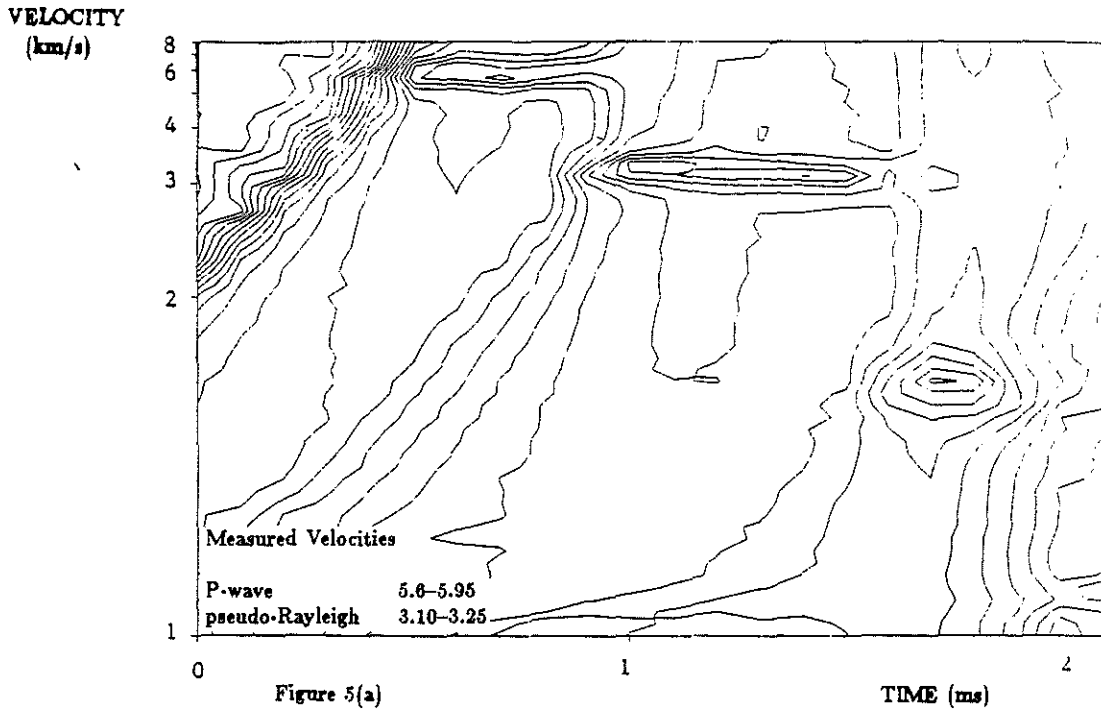


Figure 5: Velocity analysis for the model in Fig. 4. $T = 250 \mu\text{s}$; $d\tau = 100 \mu\text{s}$; $df = 4$ kHz. (a) Velocity spectrum at 4 kHz. (b) Velocity spectrum at 8 kHz. (c) Velocity spectrum at 16 kHz. (d) Semblance.

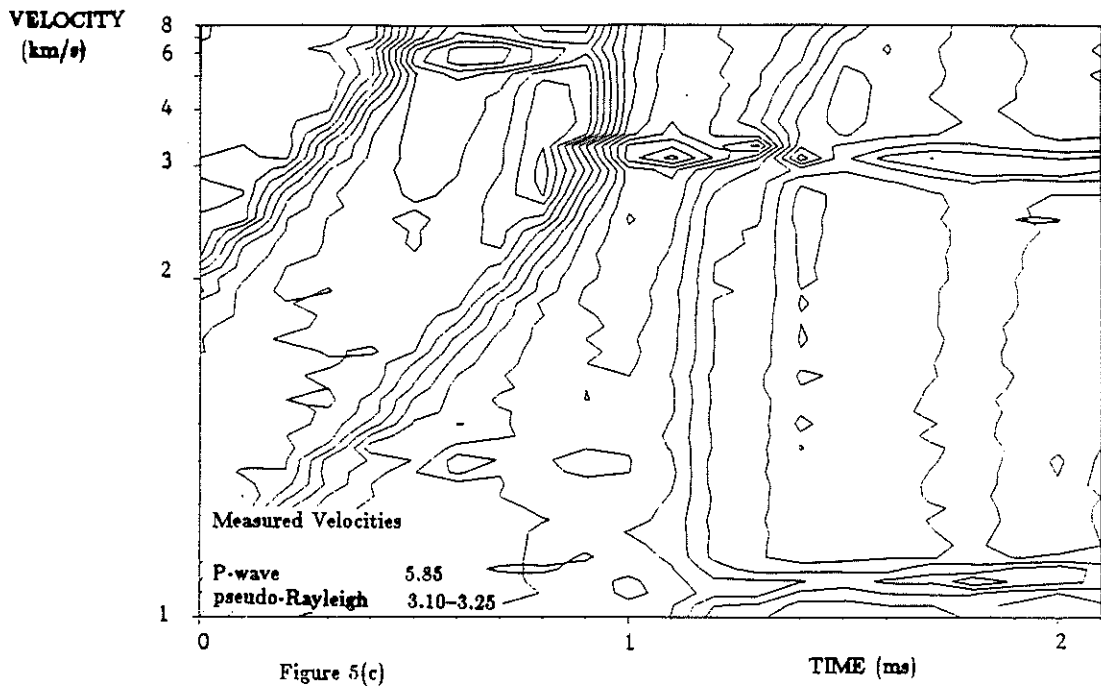


Figure 5(c)

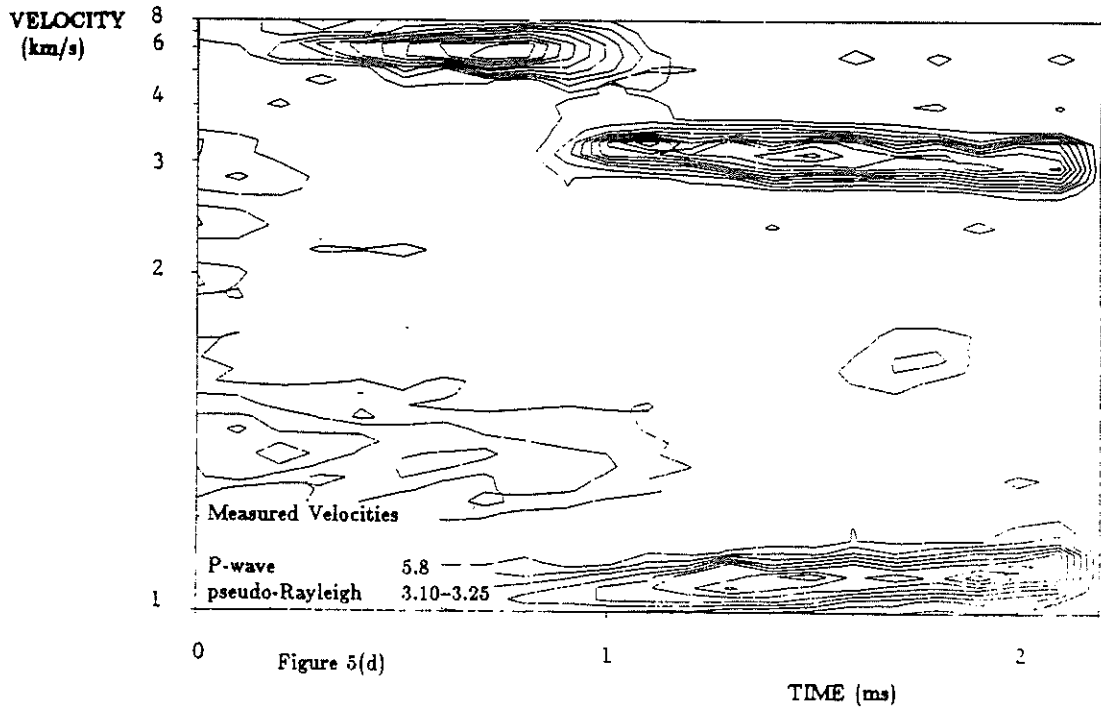
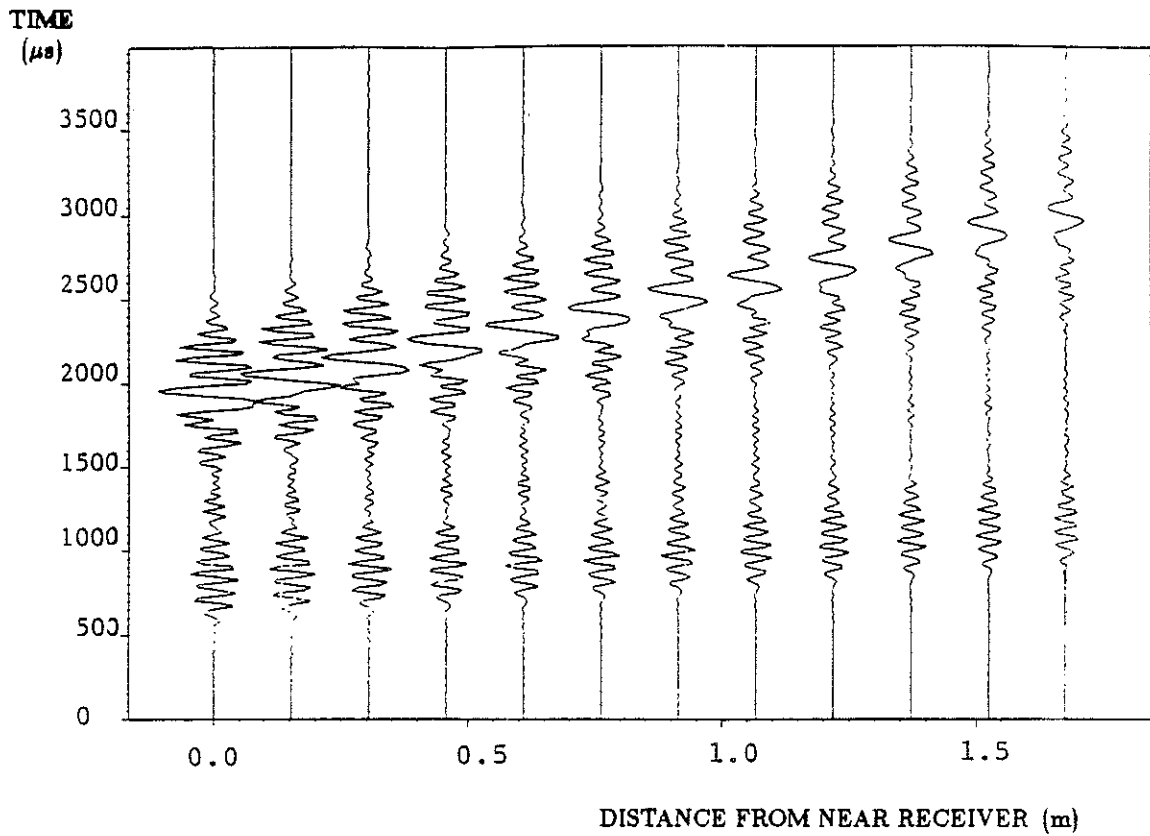


Figure 5(d)



MODEL PARAMETERS

LAYER	OUTER RADIUS (cm)	V_p (km/s)	V_s (km/s)	DENSITY (g/cc)	Q_p	Q_s
fluid	4.699	1.68	0.00	1.20	20.00	0.00
steel	5.715	6.10	3.35	7.50	1000.00	1000.00
fluid	6.985	1.68	0.00	1.20	20.00	0.00
cement	10.160	2.82	1.73	1.92	40.00	30.00
formation	∞	4.00	2.13	2.16	60.00	60.00

sampling interval = 15.625 μ s

Figure 6: Data for a free pipe model with a 1.27 cm-thick fluid layer.

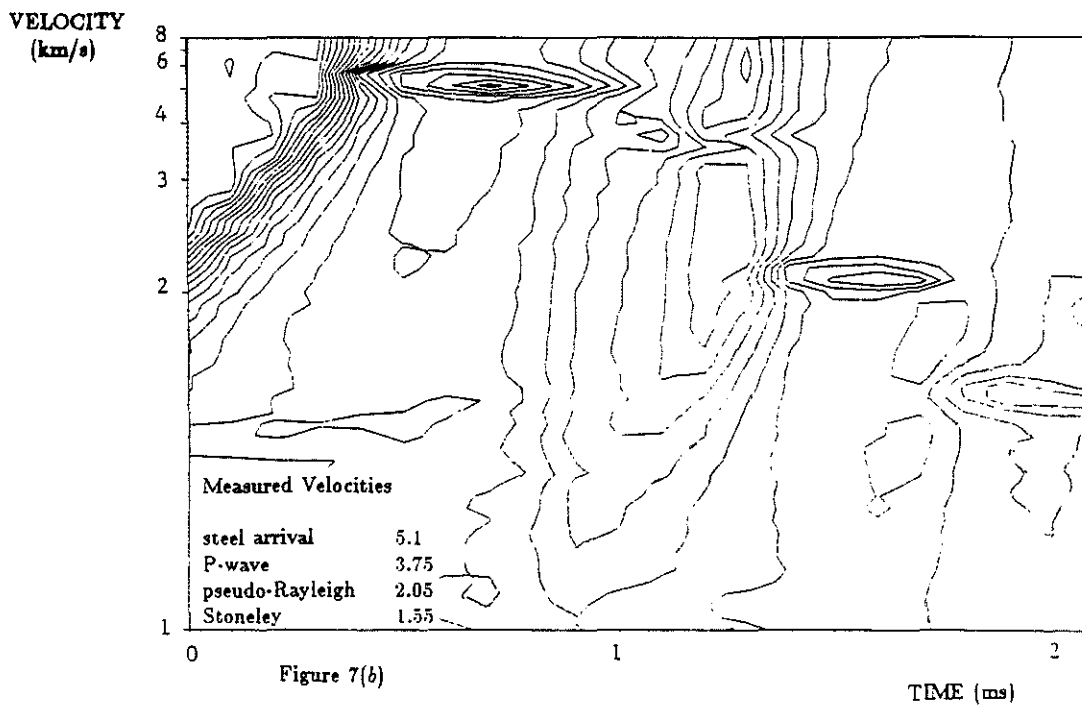
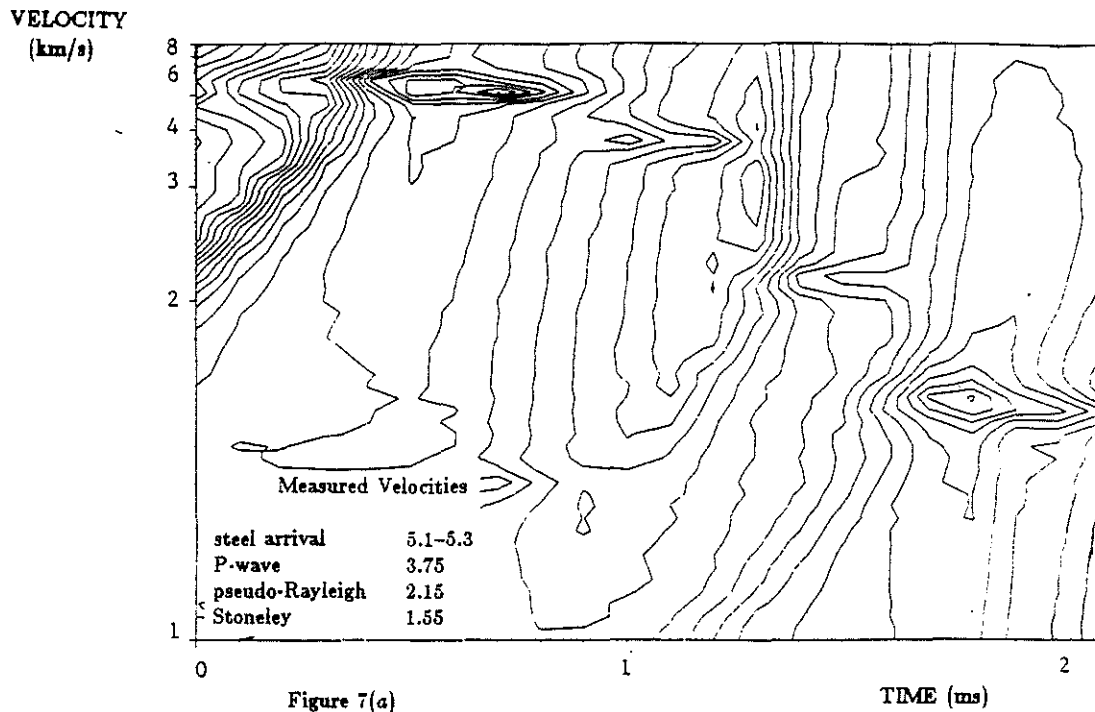
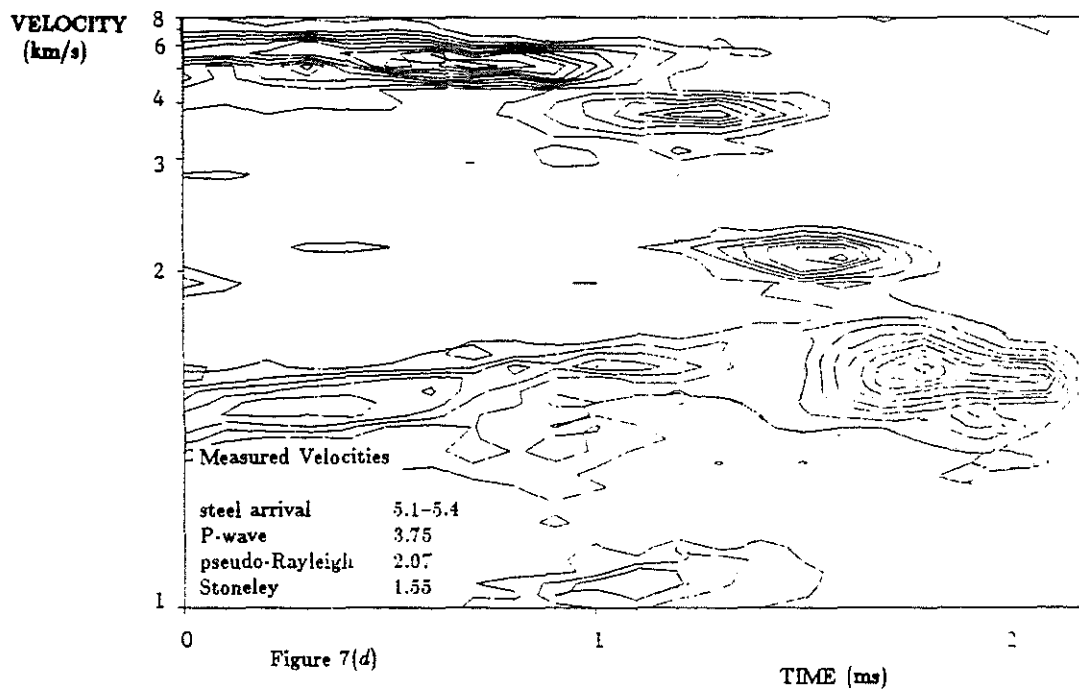
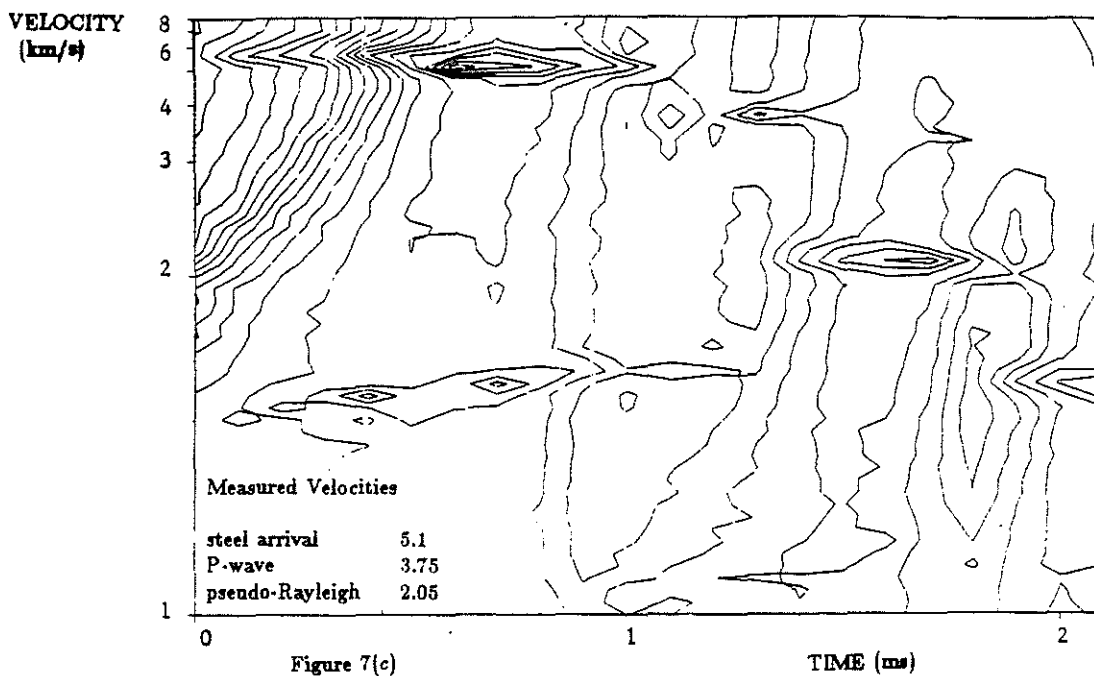
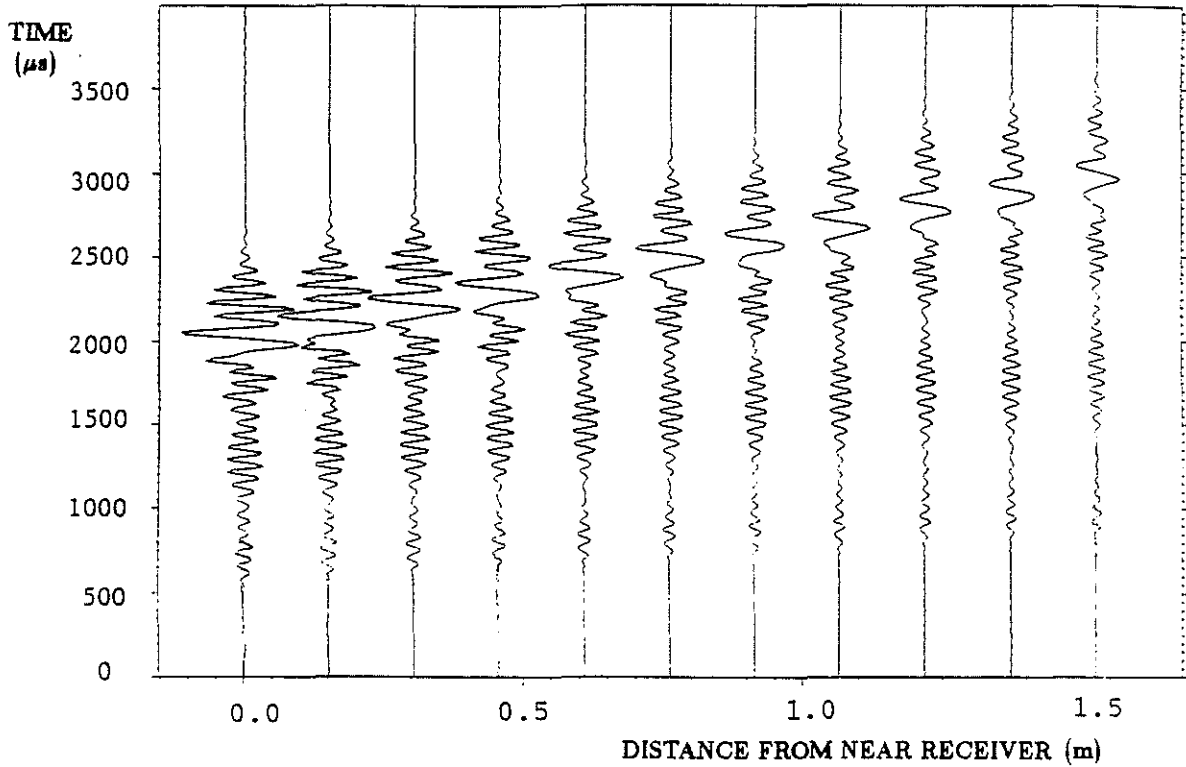


Figure 7: Velocity analysis for the model in Fig. 6. $T = 250 \mu\text{s}$; $d\tau = 100 \mu\text{s}$; $df = 4 \text{ kHz}$.
 (a) Velocity spectrum at 8 kHz. (b) Velocity spectrum at 12 kHz. (c) Velocity spectrum at 16 kHz. (d) Semblance.





MODEL PARAMETERS

LAYER	OUTER RADIUS (cm)	V_p (km/s)	V_s (km/s)	DENSITY (g/cc)	Q_p	Q_s
fluid	4.699	1.68	0.00	1.20	20.00	0.00
steel	5.715	6.10	3.35	7.50	1000.00	1000.00
fluid	5.7175	1.68	0.00	1.20	20.00	0.00
cement	10.160	2.82	1.73	1.92	40.00	30.00
formation	∞	4.00	2.13	2.16	60.00	60.00

sampling interval = 13.333334 μs

Figure 8: Data for a free pipe model with a microannulus. The formation parameters are the same as those in Fig. 6.

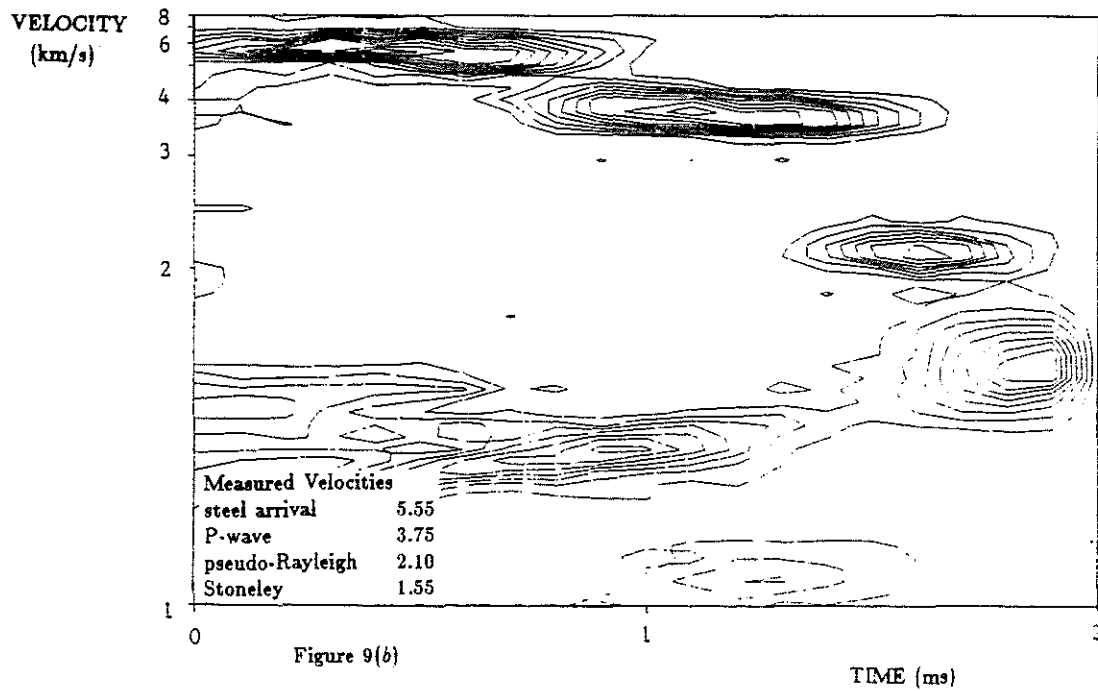
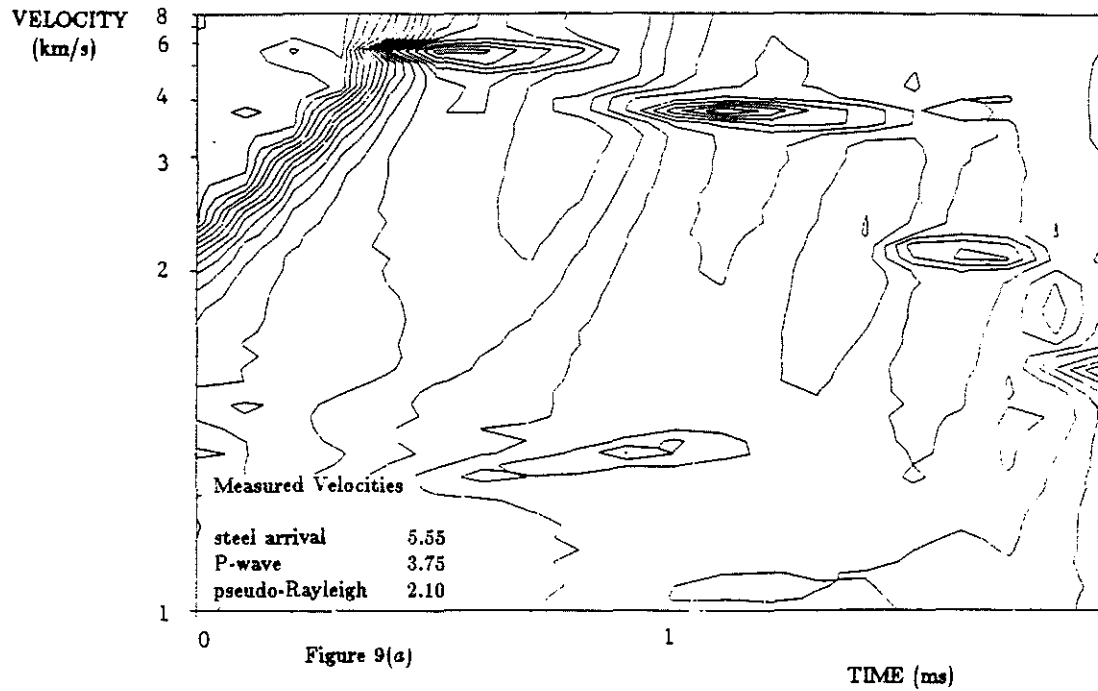
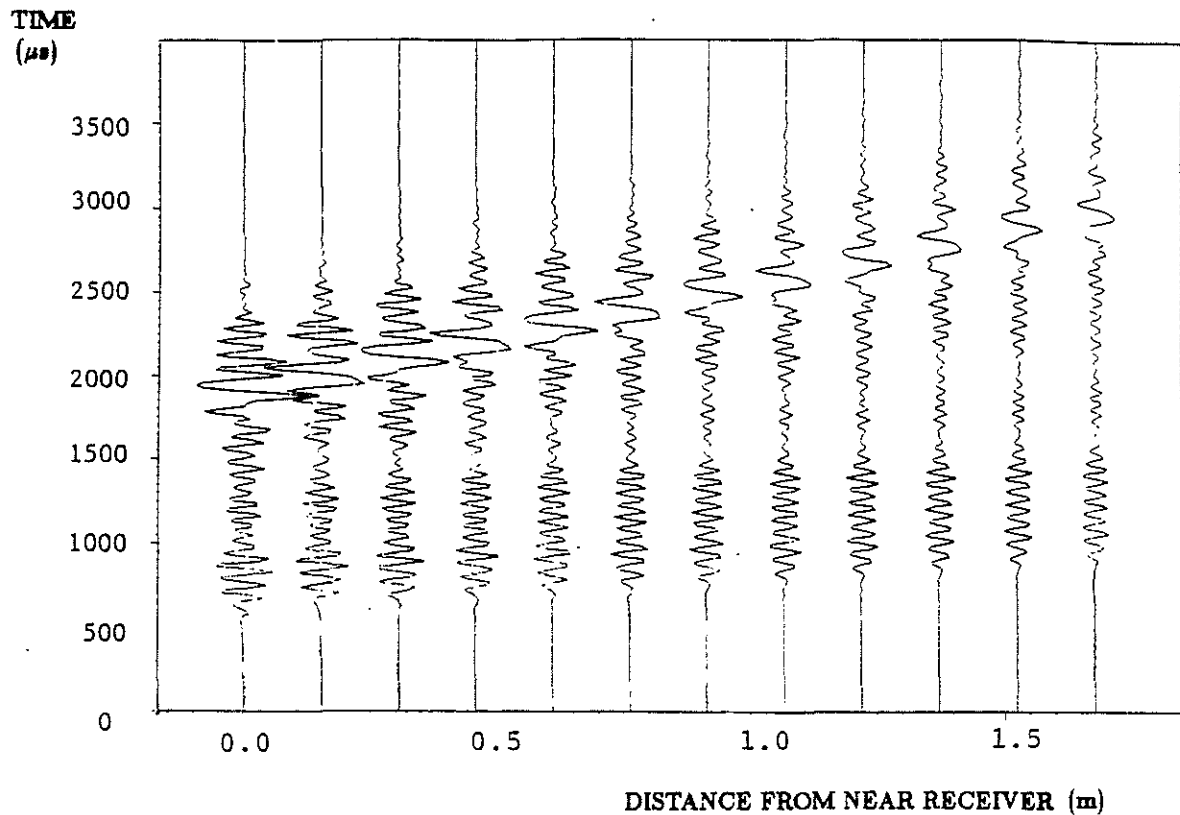


Figure 9: Velocity analysis for the model in Fig. 8. $T = 250 \mu\text{s}$; $d\tau = 100 \mu\text{s}$; $df = 2.5$ kHz. (a) Velocity spectrum at 11.7 kHz. (b) Semblance.



MODEL PARAMETERS

LAYER	OUTER RADIUS (cm)	V_p (km/s)	V_s (km/s)	DENSITY (g/cc)	Q_p	Q_s
fluid	4.699	1.68	0.00	1.20	20.00	0.00
steel	5.715	6.10	3.35	7.50	1000.00	1000.00
fluid	6.985	1.68	0.00	1.20	20.00	0.00
cement	10.160	2.82	1.73	1.92	40.00	30.00
formation	∞	4.88	2.60	2.16	60.00	60.00

sampling interval = 15.625 μs

Figure 10: Data for a free pipe model with a 1.27 cm-thick fluid layer. The borehole geometry is the same as that in Fig. 6, but the formation velocities are higher.

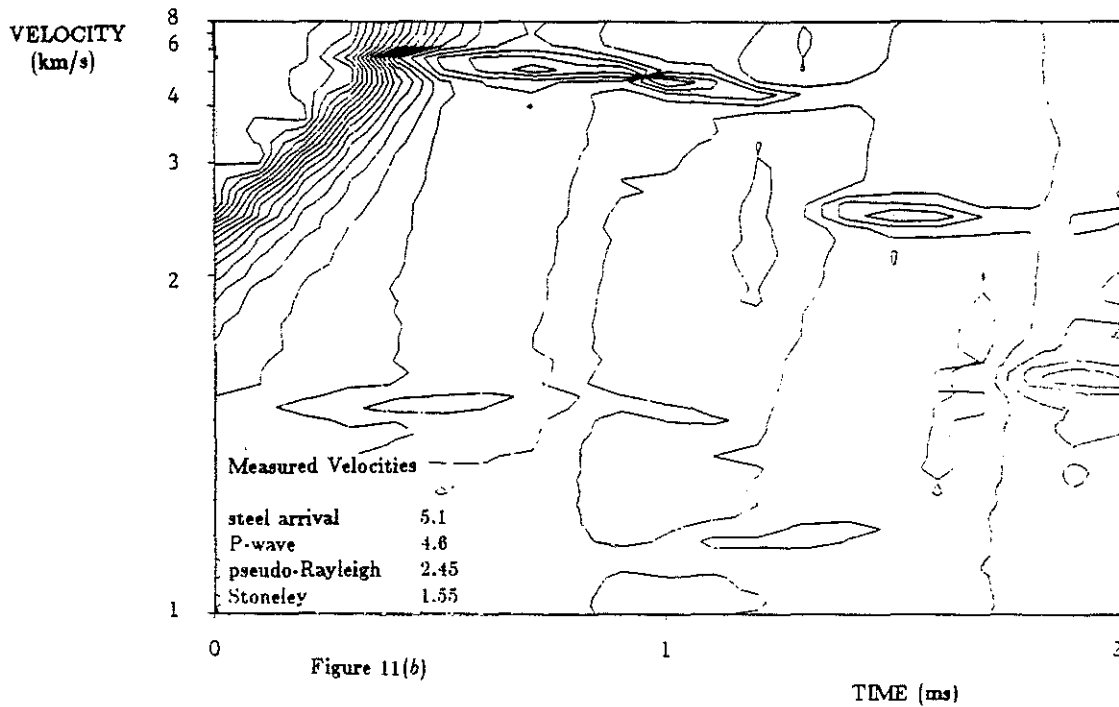
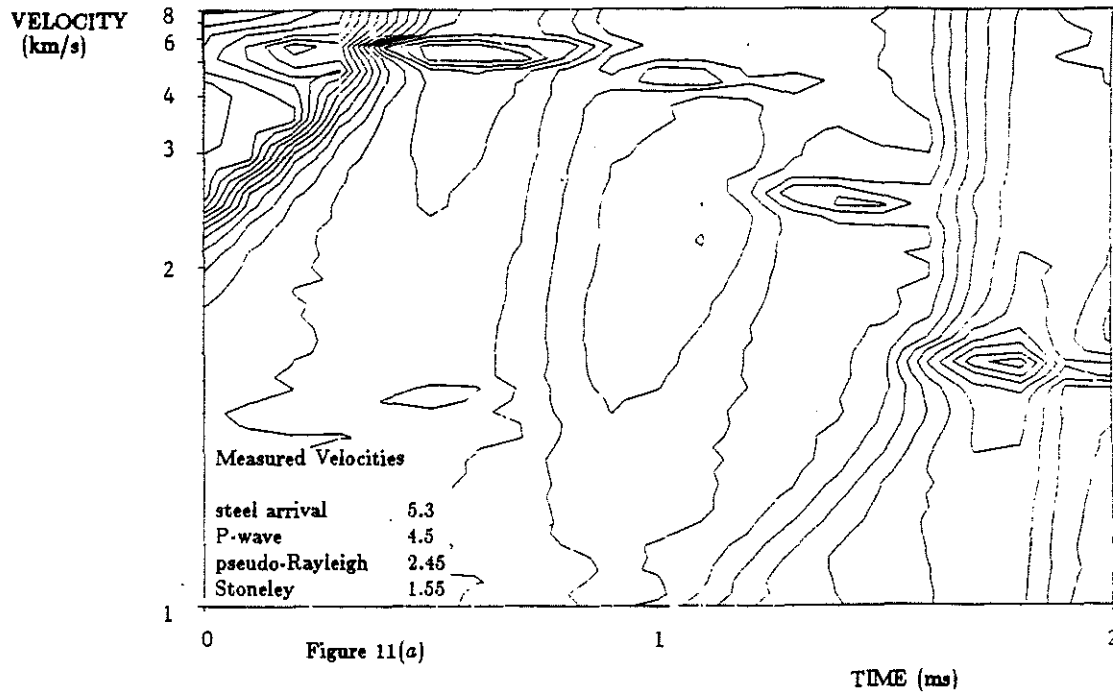


Figure 11: Velocity analysis for the model in Fig. 10. $T = 250 \mu\text{s}$; $d\tau = 100 \mu\text{s}$; $df = 4 \text{ kHz}$. (a) Velocity spectrum at 8 kHz. (b) Velocity spectrum at 12 kHz. (c) Velocity spectrum at 16 kHz. (d) Semblance.

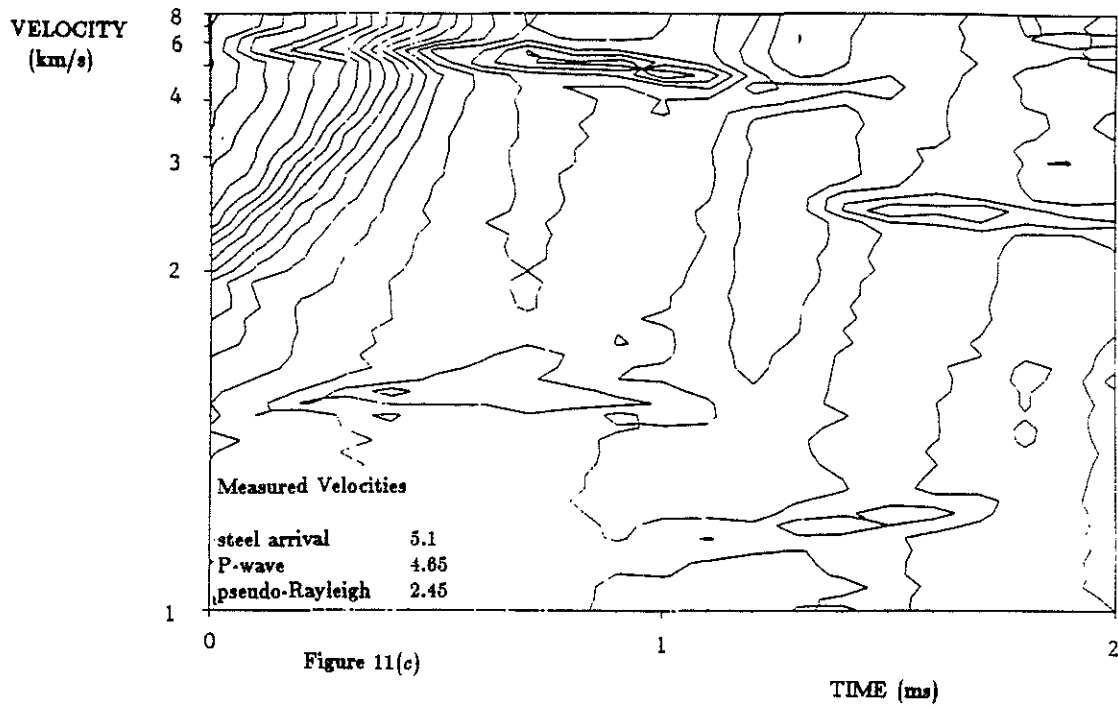


Figure 11(c)

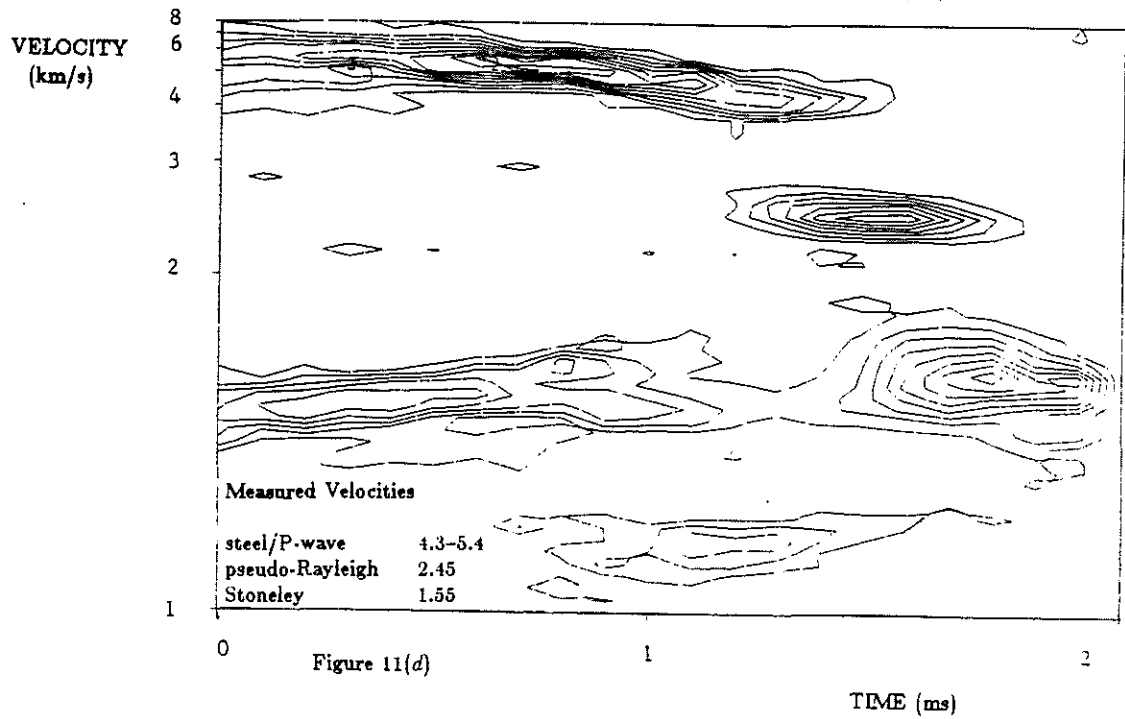
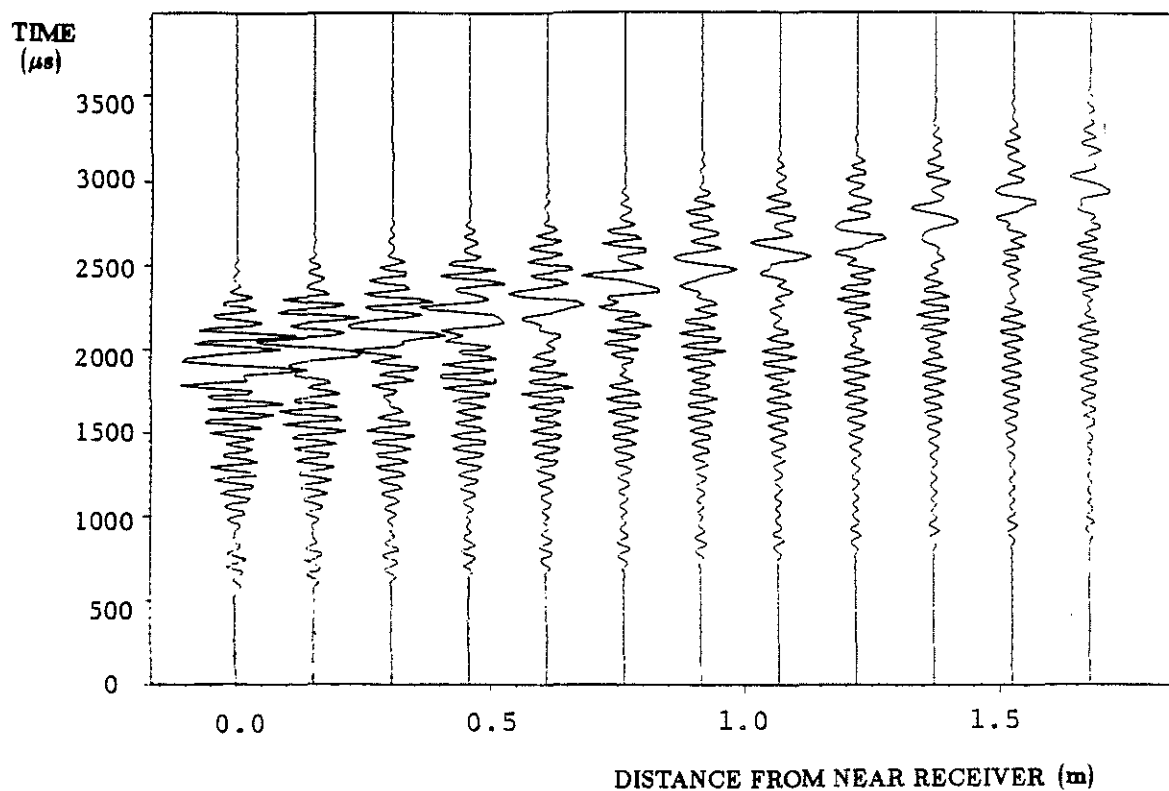


Figure 11(d)



MODEL PARAMETERS

LAYER	OUTER RADIUS (cm)	V_p (km/s)	V_s (km/s)	DENSITY (g/cc)	Q_p	Q_s
fluid	4.699	1.68	0.00	1.20	20.00	0.00
steel	5.715	6.10	3.35	7.50	1000.00	1000.00
fluid	5.7175	1.68	0.00	1.20	20.00	0.00
cement	10.160	2.82	1.73	1.92	40.00	30.00
formation	∞	4.88	2.60	2.16	60.00	60.00

sampling interval = 15.625 μ s

Figure 12: Data for a free pipe model with a microannulus. The formation parameters are the same as those in Fig. 10. The borehole geometry is the same as that in Fig. 8.

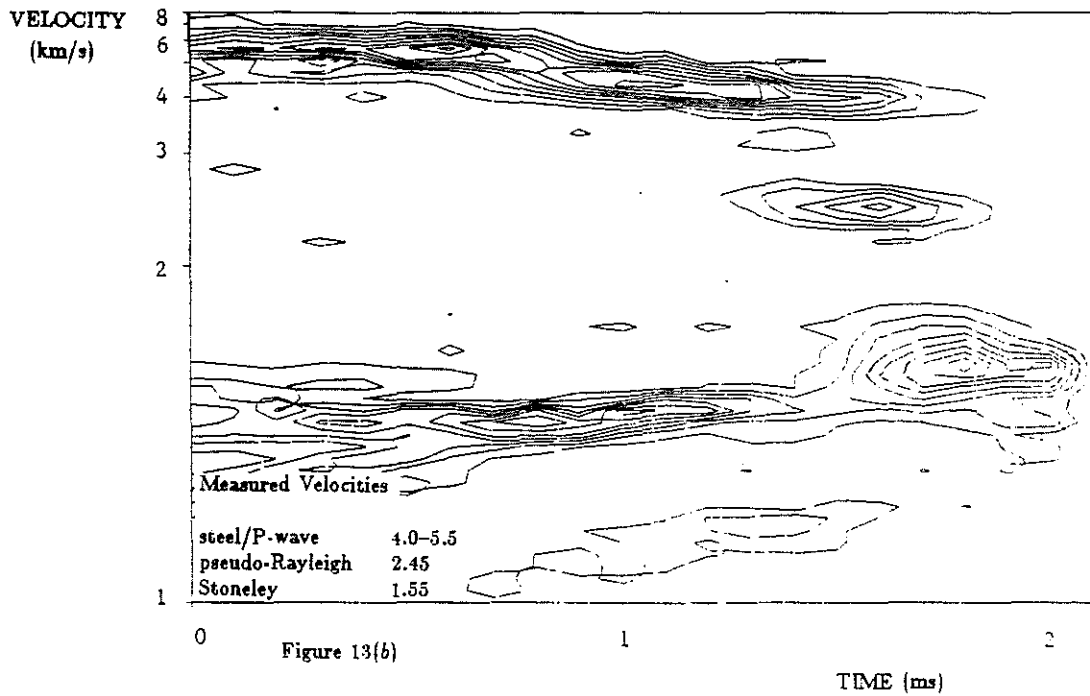
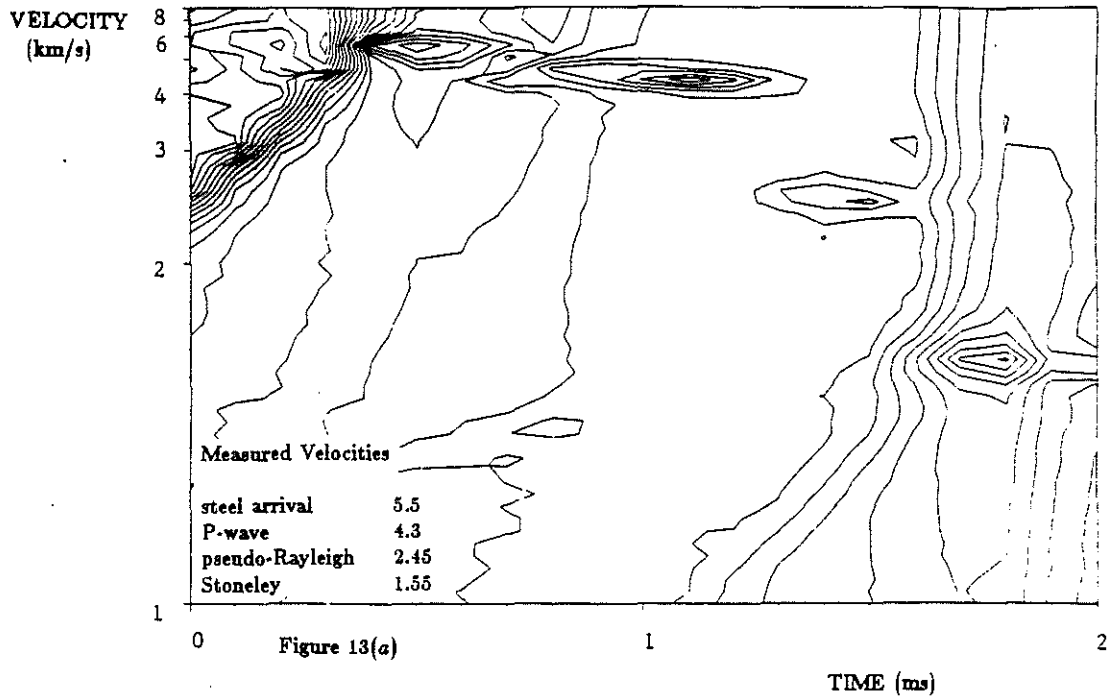
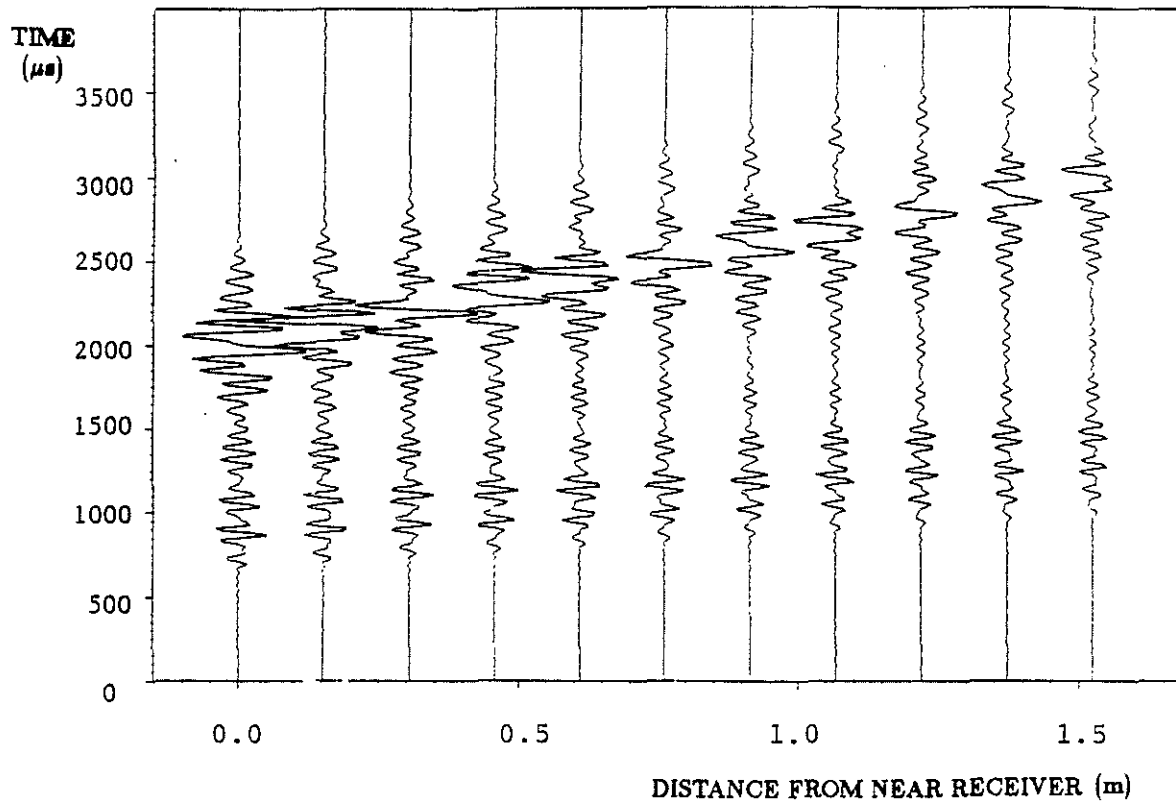


Figure 13: Velocity analysis for the model in Fig. 12. $T = 250 \mu\text{s}$; $d\tau = 100 \mu\text{s}$; $df = 4 \text{ kHz}$. (a) Velocity spectrum at 8 kHz. (b) Semblance.



MODEL PARAMETERS

LAYER	OUTER RADIUS (cm)	V_p (km/s)	V_s (km/s)	DENSITY (g/cc)	Q_p	Q_s
fluid	4.699	1.88	0.00	1.20	20.00	0.00
steel	5.715	6.10	3.35	7.50	1000.00	1000.00
cement	6.985	2.82	1.73	1.92	40.00	30.00
fluid	10.160	1.88	0.00	1.20	20.00	0.00
formation	∞	4.00	2.13	2.16	60.00	60.00

sampling interval = 13.333334 μ s

Figure 14: Data for an unbonded casing model.

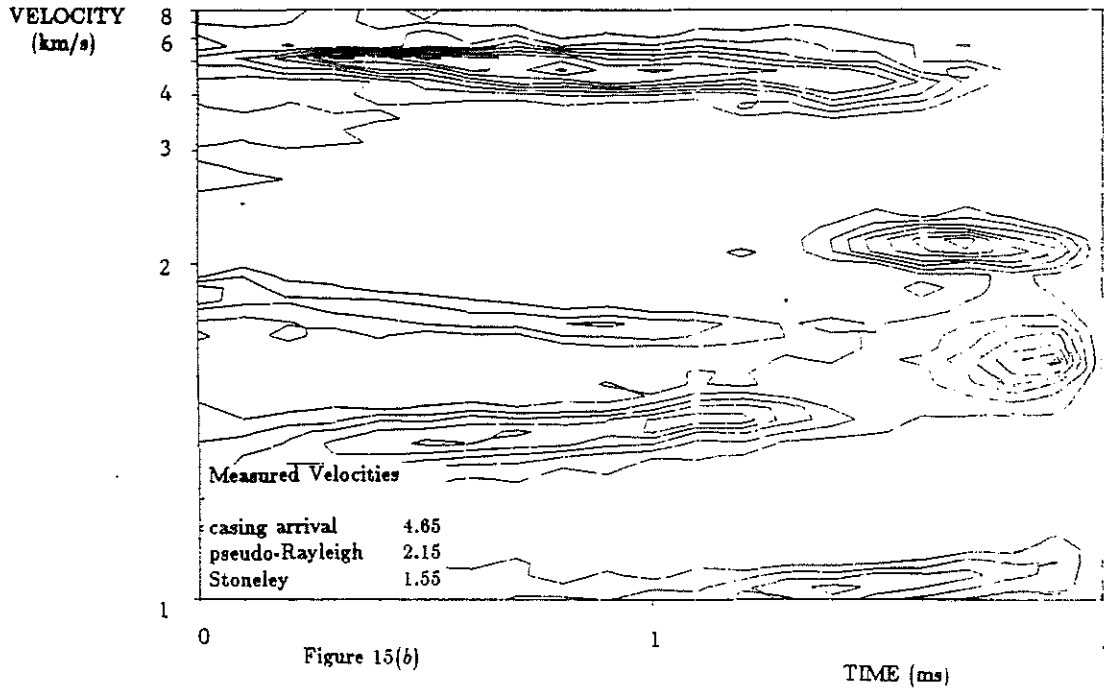
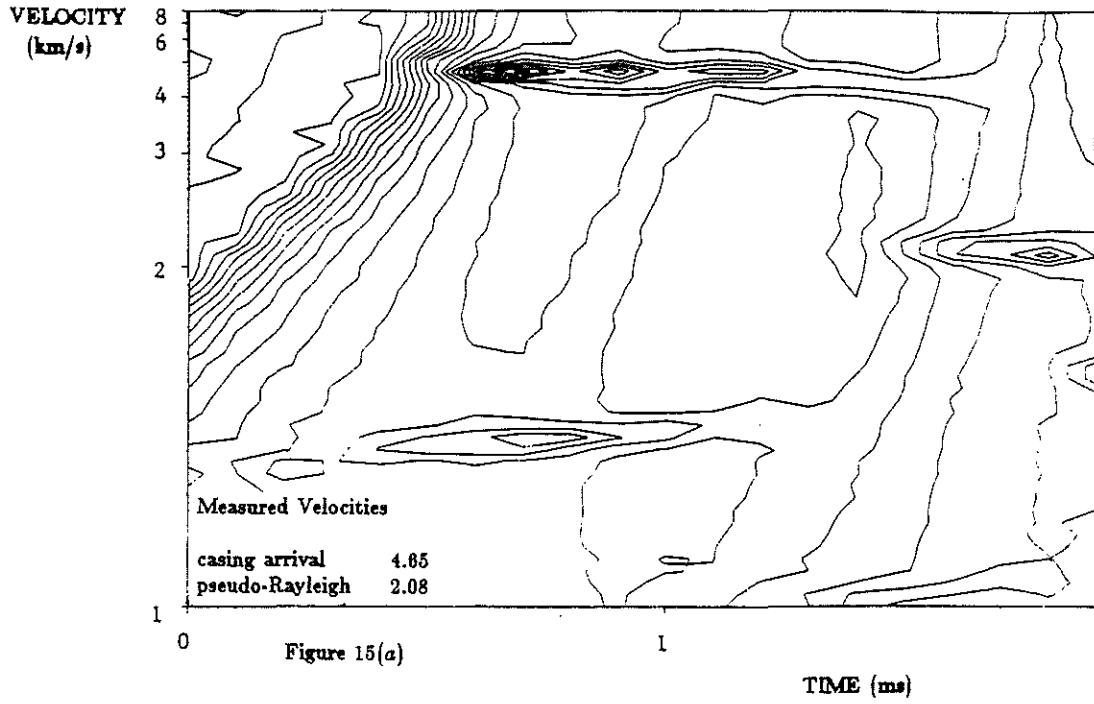
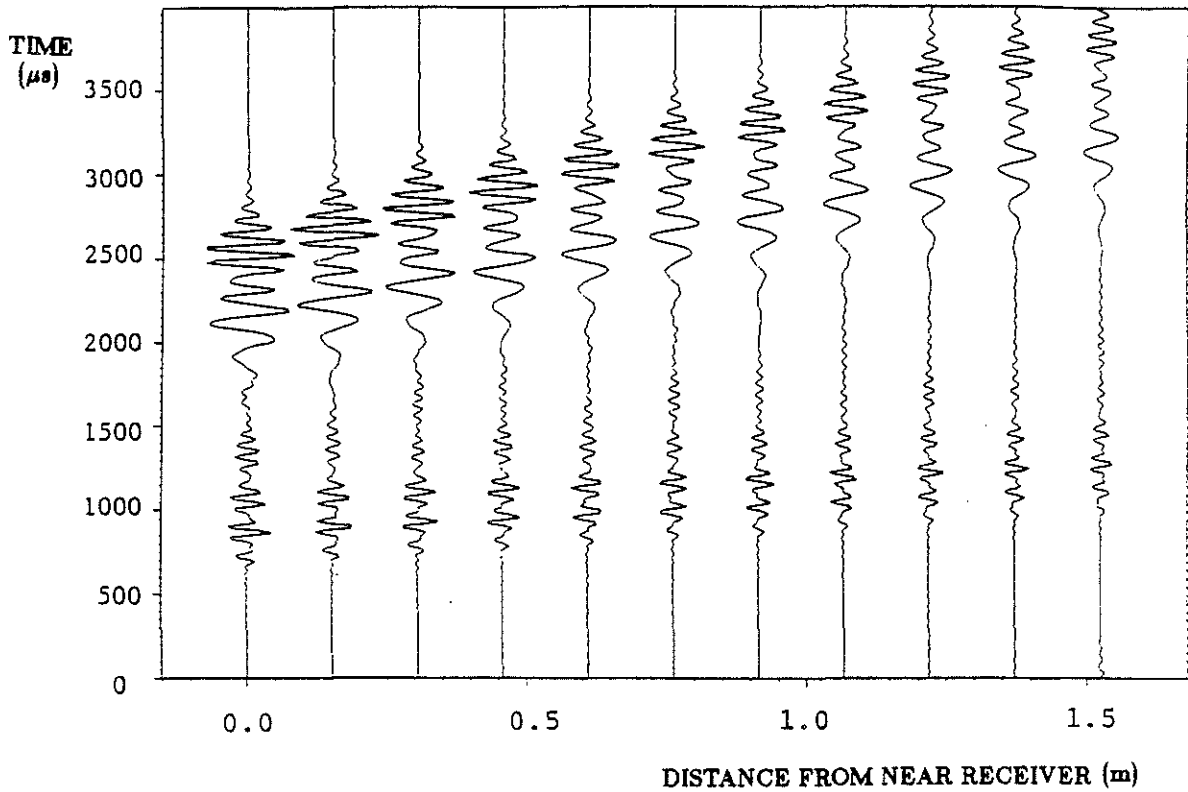


Figure 15: Velocity analysis for the model in Fig. 14. $T = 250 \mu\text{s}$; $dr = 100 \mu\text{s}$; $df = 2.5$ kHz. (a) Velocity spectrum at 11.7 kHz. (b) Semblance.



MODEL PARAMETERS

LAYER	OUTER RADIUS (cm)	V_p (km/s)	V_s (km/s)	DENSITY (g/cc)	Q_p	Q_s
fluid	4.699	1.68	0.00	1.20	20.00	0.00
steel	5.715	6.10	3.35	7.50	1000.00	1000.00
cement	6.985	2.82	1.73	1.92	40.00	30.00
fluid	10.160	1.68	0.00	1.20	20.00	0.00
formation	∞	2.90	1.52	2.00	100.00	50.00

sampling interval = 13.333334 μs

Figure 16: Data for an unbonded casing model in a slow formation.

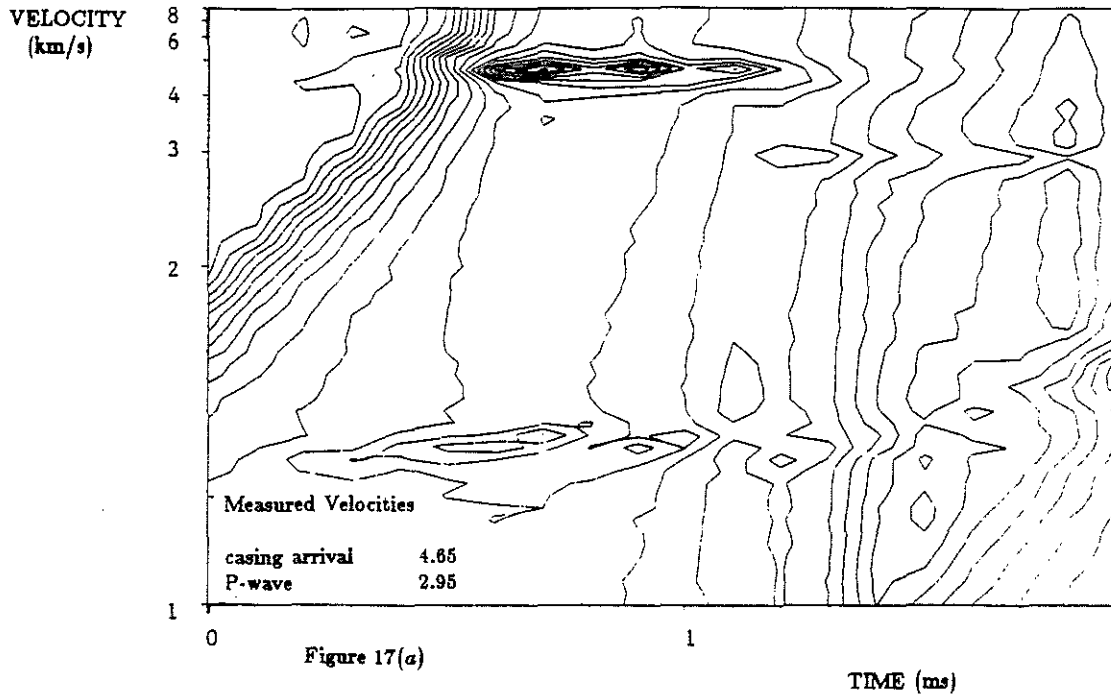


Figure 17(a)

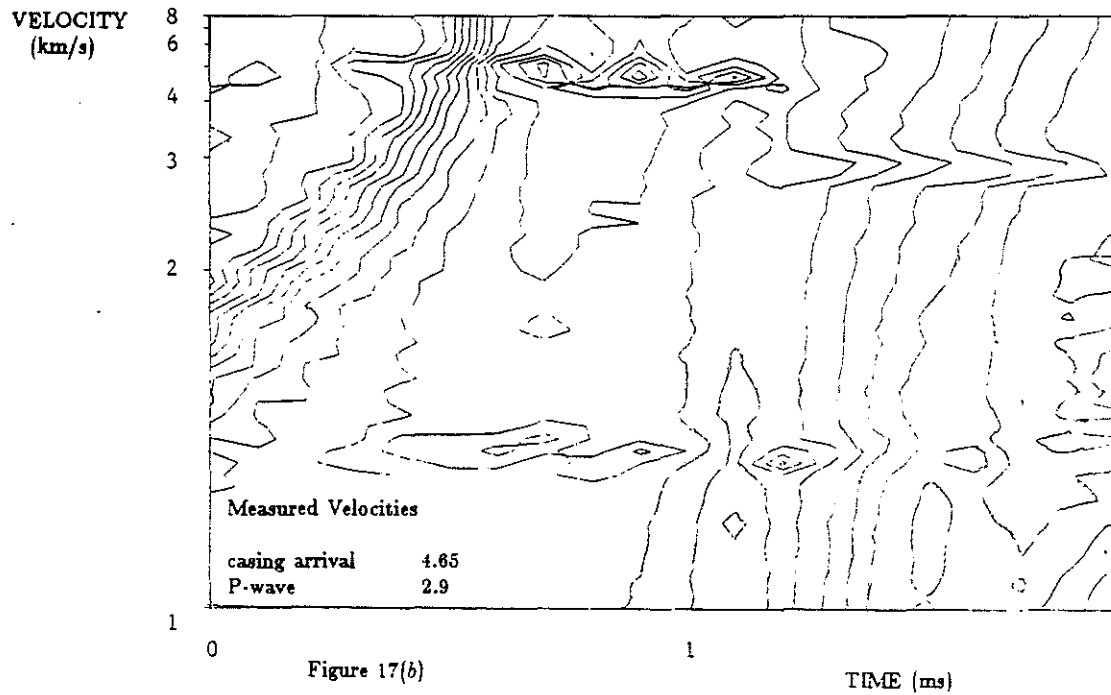
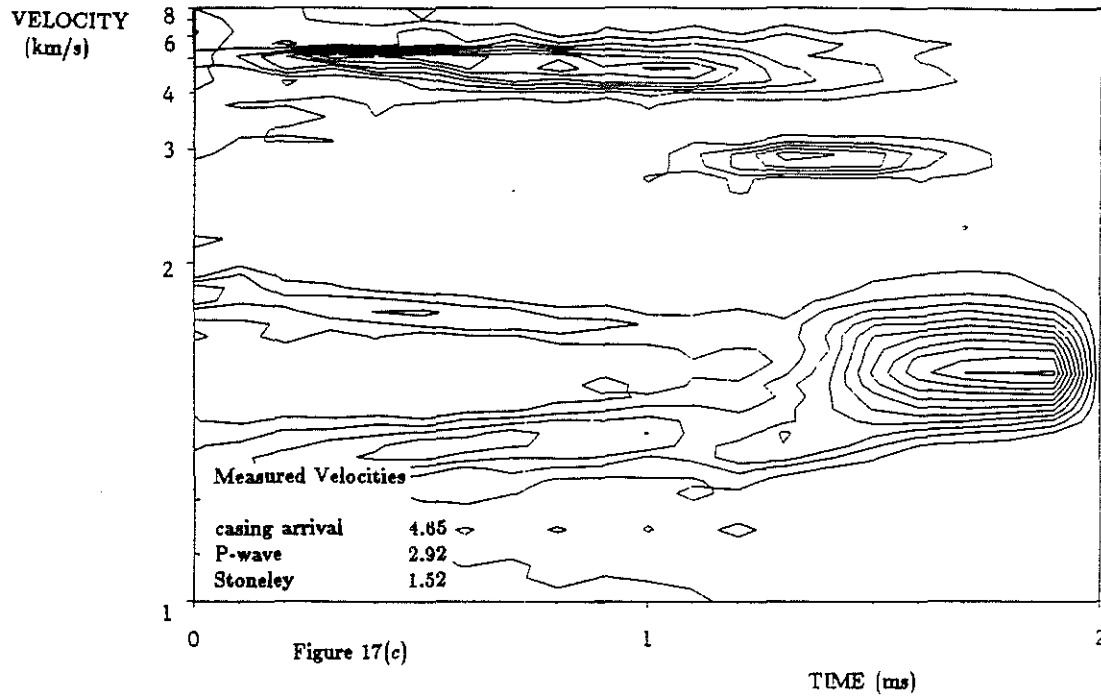


Figure 17(b)

Figure 17: Velocity analysis for the model in Fig. 16. $T = 250 \mu\text{s}$; $dr = 100 \mu\text{s}$; $df = 2.5$ kHz. (a) Velocity spectrum at 11.7 kHz. (b) Velocity spectrum at 14.1 kHz. (c) Semblance.



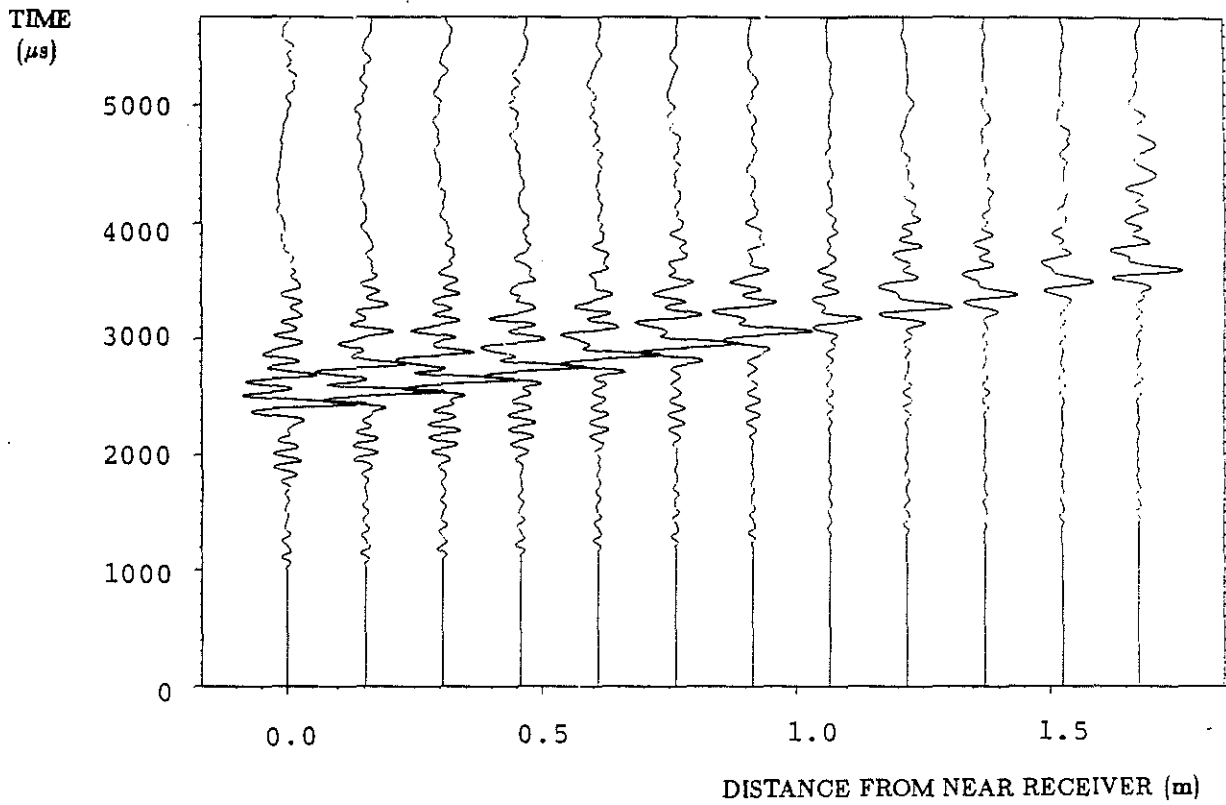


Figure 18: Field data recorded with Schumberger's Ridgefield tool in an open borehole.

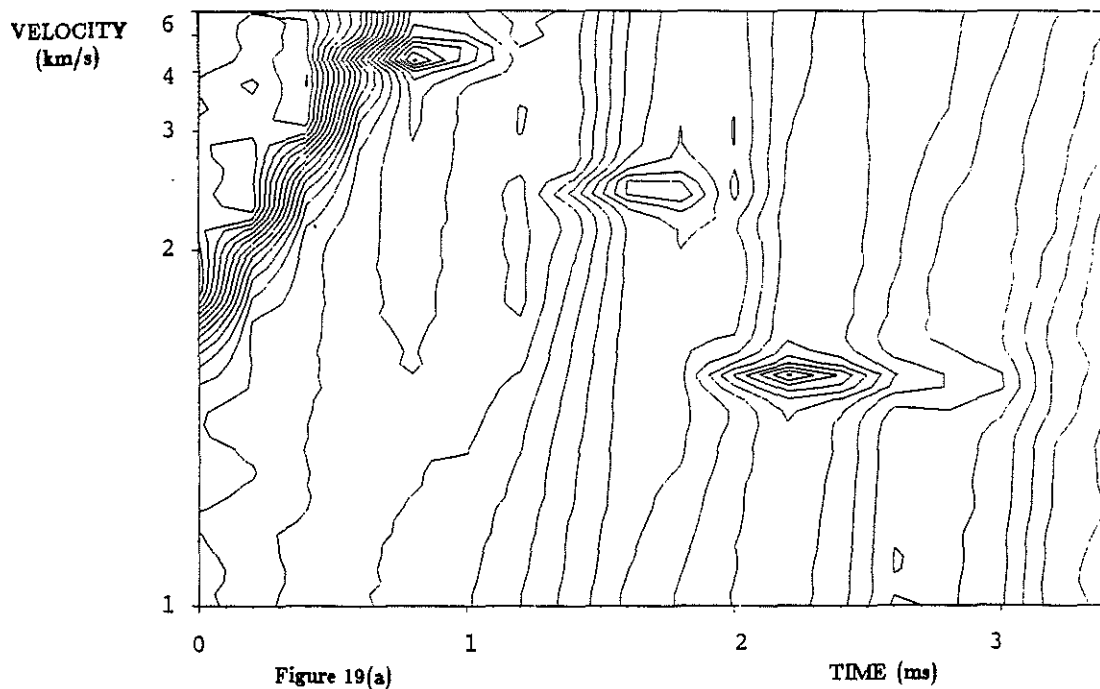


Figure 19(a)

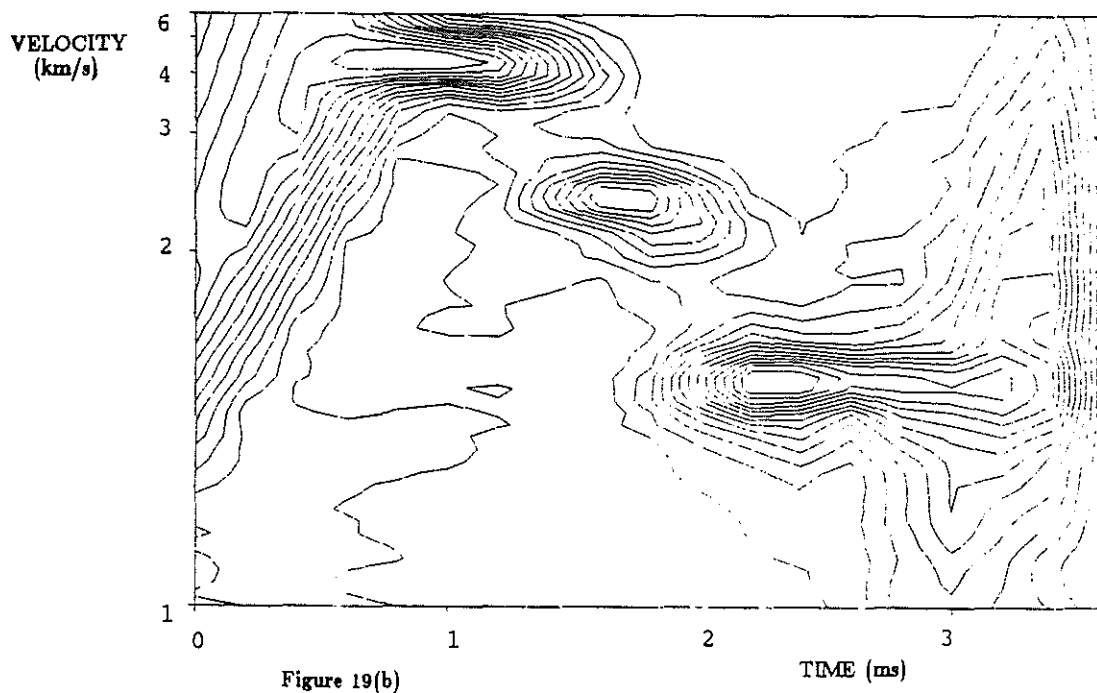


Figure 19(b)

Figure 19: Velocity analysis of the data in Fig. 18. $T = 500 \mu\text{s}$; $dr = 200 \mu\text{s}$; $df = 2$ kHz. (a) Velocity spectrum at 9.4 kHz. (b) Semblance.